JOURNAL OF GEOPHYSICAL RESEARCH, VOL. 112, E01001, doi:10.1029/2005JE002517, 2007

TES and THEMIS study of proposed paleolake basins within the Aeolis quadrangle of Mars

Karen R. Stockstill,[1,2] Jeffrey E. Moersch,[1] Harry Y. McSween Jr.,[1] Jennifer Piatek,[1] and Philip R. Christensen[3]

Received 23 June 2005; revised 1 June 2006; accepted 29 August 2006; published 6 January 2007.

[1] Several studies have described photogeologic evidence for paleolacustrine basins on Mars, mostly within impact craters. If these basins contained persistent standing water subsequently lost through evaporation, they may have contained deposits of evaporite minerals. If still present and sufficiently exposed, these evaporites would be detectable in orbital thermal infrared spectra. Using data from Mars Orbiter–Thermal Emission Imaging System (MO-THEMIS) and Mars Global Surveyor–Thermal Emission Spectrometer (MGS-TES), we examined proposed paleolake basins within Aeolis quadrangle, including Gusev and Gale craters. Gusev Crater is dominated by units with a spectrally intermediate to thick layer of dust mantling the surface. TES linear deconvolutions of the low-albedo deposits, which have a thinner dust mantling, include Surface Type 1 (basalt) materials when sulfates are included in the end-member library. Otherwise, the linear deconvolution uses Surface Type 2 (andesite or weathered basalt). THEMIS surface emissivity spectra for the low-albedo deposits do not display sufficient contrast to distinguish between Surface Types. Gale Crater is relatively dust-free, except for the mound variably covered in a spectrally intermediate to thick layer of dust. TES linear deconvolutions of crater floor and less dusty portion of the mound are consistent with a mixture of Surface Types 1 and 2. THEMIS surface emissivity spectra are consistent with Surface Type 1 or a mixture of Surface Types 1 and 2 for the crater floor and surface dust for the mound. These results do not discriminate between several previously suggested origins (fluvial-lacustrine, aeolian, or volcanic deposition) for the mound layers. We find no spectral evidence for evaporite deposits that might substantiate paleolakes existed in these craters.

Citation: Stockstill, K. R., J. E. Moersch, H. Y. McSween Jr., J. Piatek, and P. R. Christensen (2007), TES and THEMIS study of proposed paleolake basins within the Aeolis quadrangle of Mars, *J. Geophys. Res.*, *112*, E01001, doi:10.1029/2005JE002517.

1. Introduction and Background

1.1. Water on Mars

[2] Under current temperature and pressure conditions at the surface of Mars, liquid water is not stable and will rapidly evaporate or freeze [e.g., *Mutch et al.*, 1976; *Carr*, 1987]. However, a number of geomorphic features suggest that the climatic conditions of early Mars may have been quite different, allowing abundant and persistent liquid water to have existed [e.g., *Carr*, 1996]. For example, the high degree of erosion of large impact craters and dissection of the oldest terrain by large channels and smaller ''valley networks'' provide compelling evidence that early Mars was indeed warmer and wetter than at present. Many authors suggest that the channels on Mars were formed by catastrophic floods, whereas the valley networks were formed by surface runoff or groundwater sapping [e.g., *Masursky*, 1973; *Milton*, 1973; *Sagan et al.*, 1973; *Baker and Milton*, 1974; *Sharp and Malin*, 1975]. Other studies have argued for the existence of paleolake basins on the basis of photogeologic evidence [*Forsythe and Zimbelman*, 1995; *Cabrol and Grin*, 1999; *Malin and Edgett*, 2000]. In fact, the sedimentary layers described by *Malin and Edgett* [2000] are found within some of the proposed paleolake basins studied in the present work.

[3] *Cabrol and Grin* [1999] presented a survey of 179 possible paleolake basins in Martian impact craters. These basins were classified according to their relationship to neighboring basins and the types of associated channels. For each basin, the survey identified specific lines of geomorphic and photogeologic evidence used to support a paleolake hypothesis. This evidence included bands of alternating light and dark albedo material conformable with a basin's margin or bright materials exposed in the central portion of the basin, which *Cabrol and Grin* [1999] interpreted as possible evaporite deposits. On Earth, playa basin

[1]Department of Earth and Planetary Sciences, University of Tennessee, Knoxville, Tennessee, USA.
[2] Now at HIGP/UH-NAI, University of Hawaii at Manoa, Honolulu, Hawaii, USA.
[3] Department of Geological Sciences, Arizona State University, Tempe, Arizona, USA.

0148-0227/07/2005JE002517$09.00

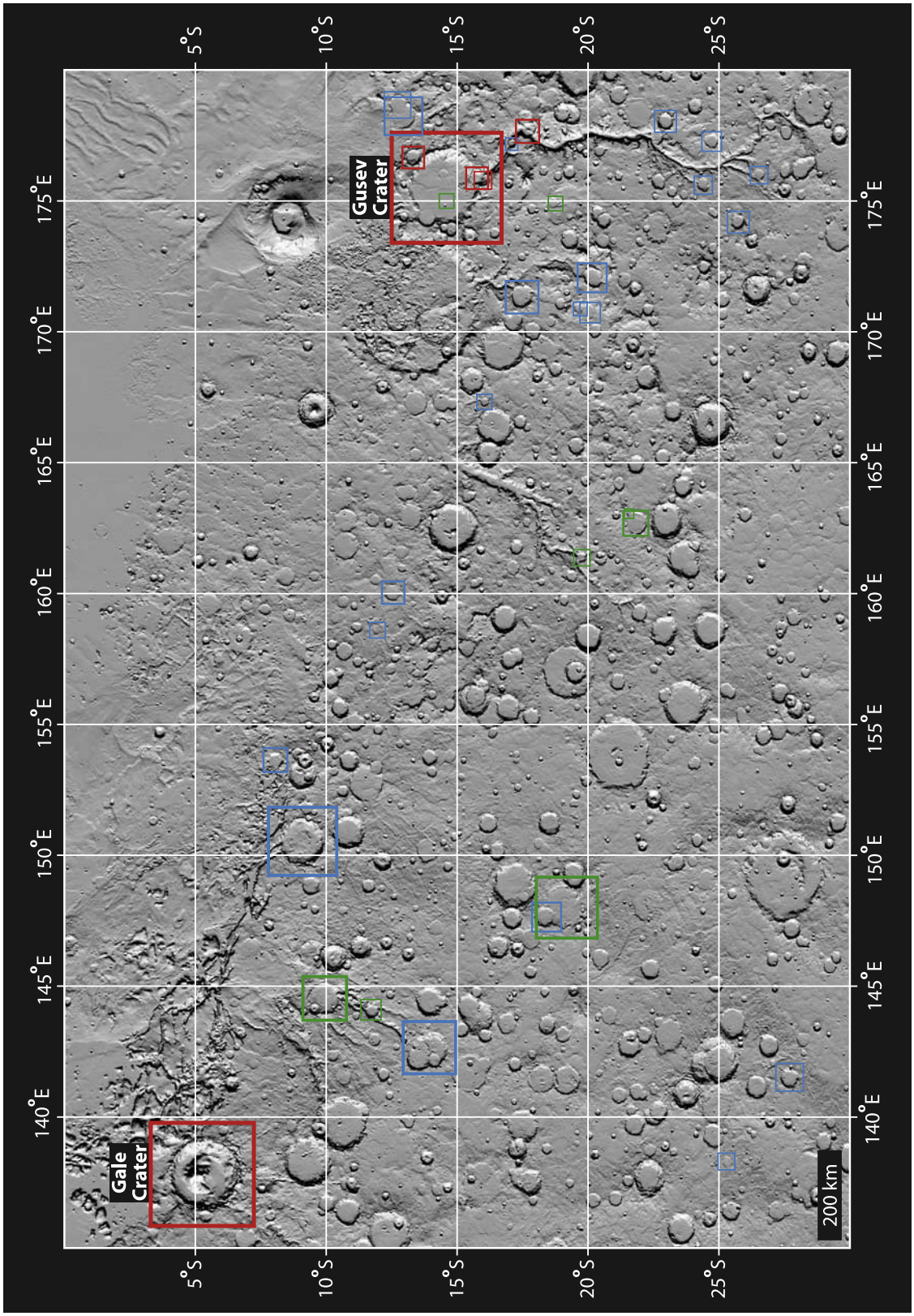
Gusev Crater
Gale Crater
200 km
5°S
10°S
15°S
20°S
25°S
140°E
145°E
150°E
155°E
160°E
165°E
170°E
175°E

Figure 1

evaporites often display a characteristic (bull's-eye) spatial pattern resulting from their order of deposition [*Jones*, 1965; *Eugster and Hardie*, 1978; *Eugster*, 1980].

1.2. Aeolis Quadrangle

[4] Thirty-five basins from the *Cabrol and Grin* [1999] list are within the Aeolis quadrangle, making it the most populated quadrangle of those represented on the list (Figure 1). In addition, this quadrangle contains both Gusev and Gale craters. Both craters were well-studied as potential landing sites for the Mars Exploration Rover (MER) missions; Gale Crater was excluded because the landing ellipse exceeded the size of the crater [*Golombek et al.*, 2002] and Gusev Crater was chosen as the landing site of Spirit rover [*Squyres et al.*, 2004]. For these reasons, we chose to use thermal infrared data of the basins within the Aeolis quadrangle to search for spectral evidence that they were once paleolakes.

[5] The Aeolis quadrangle encompasses a portion of the dichotomy boundary between the heavily cratered and dissected highlands and the relatively smooth lowlands of Mars. The heavily cratered highlands have been dated as Noachian [*Greeley and Guest*, 1987] and are dissected by Ma'adim and Al-qahira Valles as well as numerous smaller valleys [*Brakenridge*, 1990]. The northern lowlands are considered to be post–heavy bombardment and may consist of lava or sedimentary deposits [*Brakenridge*, 1990].

[6] Development of the valley network systems has been estimated to be Upper Noachian to Lower Hesperian in age [*Brakenridge*, 1990]. However, the surface deposits within Gusev and Gale craters have been dated as Early Amazonian [*Cabrol et al.*, 1998, 1999]. If these basins were lakes in the early Amazonian, this suggests that water was stable at the surface of Mars, at least episodically, for most of Martian history and was stable relatively recently. If lakes existed within craters as recently as the Early Amazonian, deposits of evaporite minerals may still be present. The two largest craters within the Aeolis quadrangle from the *Cabrol and Grin* [1999] list, Gusev and Gale craters, are presented in this paper. The results for the remaining craters studied within the Aeolis quadrangle are presented by *Stockstill* [2005].

1.2.1. Gusev Crater (14.5°S, 175.5°E)

[7] Gusev Crater is a 160 km-diameter basin located at the end of the 900 km-long Ma'adim Vallis (Figure 1) and may represent the lacustrine depocenter or terminal basin for this drainage system [*Schneeberger*, 1989; *Cabrol et al.*, 1998; *Farmer and Des Marais*, 1999]. Similar terminal lake basin settings on Earth typically have high rates of chemical sedimentation and high biological productivity and are very favorable for the preservation of biomarkers [*Farmer and Des Marais*, 1999]; if life existed on Mars in the past, Martian fluvio-lacustrine environments would be a favored setting for exploring for evidence of past Martian life.

[8] Using Mariner 9 data, *Scott et al.* [1978] mapped the surface within Gusev Crater as a moderately thick aeolian deposit covering lava flows. Investigations using Viking imagery have yielded several maps of surface units within Gusev Crater [*Landheim et al.*, 1994; *Grin and Cabrol*, 1997; *Kuzmin et al.*, 2000]. The *Landheim et al.* [1994] study identified surface units within the crater floor attributed to crater formation and fluvial deposition. *Grin and Cabrol* [1997] produced a sedimentologic map that identified surface units suggested to have formed by lacustrine and aeolian deposition. Finally, the *Kuzmin et al.* [2000] study distinguished surface units within Gusev crater that were ascribed to fluvial-lacustrine deposition.

[9] More recent investigations using data from the Thermal Emission Spectrometer (TES), Thermal Emission Imaging System (THEMIS) and Mars Orbiter Camera (MOC) data have yielded detailed maps of surface units within Gusev [*Milam et al.*, 2003; *Martínez-Alonso et al.*, 2005]. The *Milam et al.* [2003] study distinguished nine surface units within Gusev crater that were consistent with either fluvio-lacustrine, aeolian and/or volcanic deposition. However, the spatial resolution of the data did not allow for the distinction of textures diagnostic of any one type of deposition, nor did it provide unambiguous evidence for a fluvio-lacustrine depocenter [*Milam et al.*, 2003]. Utilizing the same data sets, the study by *Martínez-Alonso et al.* [2005] concluded that the current surface in Gusev Crater is consistent with volcanic (basaltic) and aeolian deposits; fluvio-lacustrine deposits proposed by other authors may be present beneath these deposits or exposed in impact craters.

[10] In addition to remote sensing studies, the MER Spirit rover has also studied Gusev Crater at its surface. The Spirit rover landed in Gusev Crater in early January of 2004 and continues to explore its surface. During the primary mission, rocks examined on the floor of Gusev Crater were found to be pristine basalts containing olivine, lacking phyllosilicates and other aqueous weathering products, but sometimes exhibiting minor surface coatings [*Christensen et al.*, 2004a; *Gellert et al.*, 2004; *McSween et al.*, 2004; *Morris et al.*, 2004]. *Morris et al.* [2004] have suggested that the presence of olivine indicates that physical, rather than chemical, weathering currently dominates the weathering processes at Gusev Crater. More recently, the Spirit rover has encountered rocks on and around Columbia Hills that are "highly altered", with decreased olivine contents and variations in the Fe oxide component consistent with the presence of water [*Klingelhöfer et al.*, 2005; *Morris et al.*, 2005; *Schröder et al.*, 2005]. Additional evidence for alteration exists within the walls of trenches dug by Spirit rover. The trench walls displayed a 10% decrease in olivine relative to the undisturbed surface at the top of the trench, but no appreciable decrease in Ca-feldspar and Ca-pyroxene, suggesting only minor alteration [*Wang et al.*, 2005]. However, the trench also contained sulfates, silica and Fe–oxides not found at the surface, suggesting a higher

Figure 1. MOLA-derived shaded relief map of the Aeolis Quadrangle of Mars. The 35 craters from the *Cabrol and Grin* [1999] list of putative paleolake basins are outlined by colored squares. Craters enclosed in red squares displayed sufficient spectral variation to permit identification of surface spectral units. The green squares enclose craters that display insufficient spectral variation or contained surfaces that were too cold to afford useful signal-to-noise ratios. The blue squares enclose craters that had inadequate THEMIS coverage.

degree of alteration [*Wang et al.*, 2005; *Arvidson et al.*, 2006]. *Wang et al.* [2005] suggested that salty materials were formed at some distant location and were redistributed to this location by impact processes. It is important to note that mini-TES aboard the Spirit rover has not detected sulfates in undisturbed surface of Gusev Crater [*Christensen et al.*, 2004a], although sulfates sorbed onto fine-grained soil particles may have been detected in small amounts (<10–15%, the detection limit of TES and mini-TES) using other instruments aboard the Spirit rover (e.g., the Alpha Particle X-ray Spectrometer and the Mössbauer spectrometer) [*Gellert et al.*, 2004; *Morris et al.*, 2005].

1.2.2. Gale Crater (5.5°S, 137.8°E)

[11] Gale Crater is a 142 km diameter crater located near the boundary of cratered uplands and lowlands in Elysium Planitia (Figure 1). Gale appears to postdate the elevation difference between the uplands and lowlands, which occurred in the middle to late Noachian [*Frey et al.*, 1998]. The northern rim of Gale Crater is 2 km lower than its southern rim due to this regional slope [*Frey et al.*, 1998]. *Cabrol and Grin* [1997] proposed that the source of water for Gale Crater was floods from the Elysium Basin overflowing the northern rim of the crater. Crater age dating for proposed lacustrine deposits suggested an early Amazonian age [*Cabrol*, 1997]. Gale crater contains a central mound with visible layering [*Cabrol and Grin*, 1999; *Malin and Edgett*, 2000; *Greeley and Guest*, 1987; *Scott and Chapman*, 1995]. The proposed origins for the mound layers include sedimentary rocks deposited in a standing lake [*Cabrol and Grin*, 1999; *Malin and Edgett*, 2000], sedimentary rocks deposited by aeolian or fluvial processes [*Greeley and Guest*, 1987; *Scott and Chapman*, 1995], interbedded lava flows [*Greeley and Guest*, 1987] and pyroclastic deposits [*Scott and Chapman*, 1995].

[12] *Pelkey and Jakosky* [2002] studied Gale Crater using MOLA (Mars Orbiter Laser Altimeter), TES, and MOC data and found that the crater floor is generally dust-free relative to the central mound. This study characterized the amount of dust cover using both TES albedo and thermal inertia measurements. Their observations require multiple formation mechanisms to explain the various surface layers within Gale Crater, including sedimentary deposition, erosion and weathering, and aeolian processes [*Pelkey and Jakosky*, 2002]. A more recent study of Gale using the THEMIS data set [*Pelkey et al.*, 2004] confirmed these observations regarding the particle sizes present in and around Gale Crater; however, the data provided more complete and detailed information. At the high spatial resolution of THEMIS, abundant small channels were discernible supporting an aqueous history for Gale. *Pelkey et al.* [2004] identified channels on the crater walls and central mound that reach the crater floor, which they interpreted to mean that the channels postdate the existence of any paleolake within Gale Crater. Their results indicated that aeolian processes have played a major role in shaping much of the present surface layer within Gale.

1.3. Thermal Infrared Spectral Data

[13] Minerals, including evaporites, have diagnostic absorption features that result from vibrational modes within the crystal in the thermal infrared spectral region (1670–200 cm^{-1} or 6–50 μm) [e.g., *Lyon*, 1965; *Lyon and Lee*, 1970; *Christensen et al.*, 1992; *Salisbury et al.*, 1994], as demonstrated in Figure 2. TES, aboard the Mars Global Surveyor, acquired infrared data with a spatial resolution of 3 × 6 km and a spectral sampling of 10-cm^{-1} ranging from ~200-cm^{-1} to ~1655-cm^{-1} (~6–50 μm) [*Christensen*, 1999]. The TES ick-averaged noise-equivalent delta temperature (NEΔT) is 0.0013 at 270 K and 1000 cm^{-1} (10 μm) [*Christensen et al.*, 1992]. THEMIS, aboard the Odyssey spacecraft, acquires infrared images with a spatial resolution of 100 m/pixel that contain ten spectral bands. These bands are centered at 9 different wavelengths ranging from ~1472–670 cm^{-1} (~6.8–14.9 μm); band 10 (at 670 cm^{-1} or 14.88 μm) will not be used in this study as it is intended for use in atmospheric studies and is obscured by atmospheric CO_2. At 245 K, the NEΔT of THEMIS is 0.9 K at ~1429 cm^{-1} (7 μm) and 0.5 K at ~1000 cm^{-1} (10 μm) [*Christensen et al.*, 2004b]. Bands 1 and 2 have identical filters centered at ~1472 cm^{-1} (~6.8 μm) in order to boost the signal-to-noise ratio in this spectral region [*Christensen et al.*, 2004b]. These are also the bands where carbonates have their deepest, broadest absorption feature centered ~1530 cm^{-1} (~6.5 μm) [*Lane and Christensen*, 1997], as shown in Figure 2. Silicates, other evaporite minerals and TES surface end-members do not exhibit absorptions at high wave number (i.e., >1250 cm^{-1} or <8 μm) [*Christensen et al.*, 1992, and references therein; *Lane and Christensen*, 1997; *Bandfield et al.*, 2000a; *Bandfield and Smith*, 2003].

[14] Because of its higher spatial resolution, THEMIS is best viewed as a spectral unit mapper, whereas TES is better at mineral identification because of its higher spectral resolution [*Christensen et al.*, 2003]. Combined, TES and THEMIS constitute a powerful tool for studying the surface of Mars. If potential small-scale outcrops are detected within the THEMIS image, a mean spectrum from the TES pixel (or pixels) covering the outcrop region can be analyzed to determine the mineralogy. By localizing a potential evaporite outcrop to a single TES observation, the spectral contribution from the carbonate would be increased, perhaps above the lower detection limits of previous techniques [*Stockstill et al.*, 2005].

1.4. Previous TES Studies of Aqueously Derived Minerals on Mars

[15] Previous global-scale studies using TES data have revealed only two mineral signatures with possible aqueous origins: coarse-grained crystalline hematite [*Christensen et al.*, 2000a] and a minor (~2 to 5 weight%) component of carbonate in globally distributed fine-grained surface dust deposits [*Bandfield et al.*, 2003]. Although carbonates may be a minor component of the surface dust deposits, a global search of TES data binned to 1 pixel per degree by *Bandfield* [2002] did not reveal any large-scale occurrences of evaporite minerals on Mars. Even an intensive study of "White Rock", a feature suggested as a candidate evaporite deposit since the days of the Mariner 9 mission [*McCauley*, 1974; *Ward*, 1979; *Zimbelman and Kieffer*, 1979; *Williams and Zimbelman*, 1994], has not revealed the spectral signatures of evaporite minerals [*Ruff et al.*, 2001].

[16] *Stockstill et al.* [2005] conducted a TES study at the spatial resolution limit of the data set (3 × 6 km) to search for in situ evaporite deposits within the 80 largest basins from the *Cabrol and Grin* [1999] list. However, surface exposures

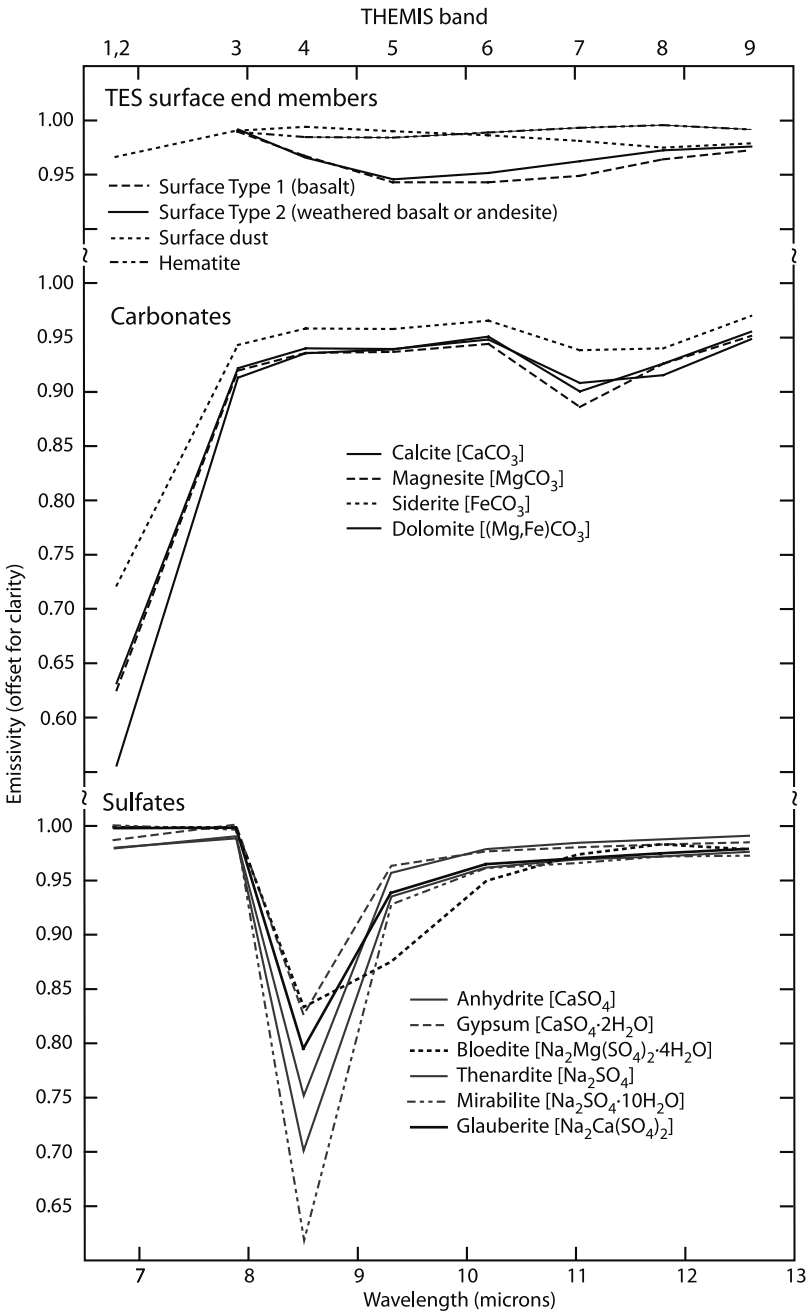

Figure 2. THEMIS resolution emissivity spectra for TES surface end-members and laboratory spectra of various rock-forming minerals that commonly form as evaporites [*Lane and Christensen*, 1997, 1998]. Note that the TES surface end-members do not have emissivity values for bands 1 and 2, as discussed in the text. *Bandfield et al.* [2003] derived the emissivity spectrum for surface dust using multiple emission angle TES data, resulting in a TES emissivity spectrum that extended to $\sim$6.0 μm.

of evaporite deposits were not detected in amounts exceeding the lower detection limits for the methods used; these methods included linear deconvolution [*Smith et al.*, 2000; *Bandfield et al.*, 2000a] and the carbonate indices technique [*Stockstill et al.*, 2005]. For linear deconvolution, the lower detection limit of sulfates is $\sim$15% [*Christensen et al.*, 2001], whereas the lower detection limit of carbonates ranges from 5% [*Christensen et al.*, 2000b; *Hamilton and Christensen*, 2000] to 10% [*Christensen et al.*, 2001; *Bandfield*, 2002]. For the carbonate indices technique, the lower detection limits ranged from 12% to 53%, depending on the carbonate species involved and the type of material with which the carbonates are spectrally mixed. That study did not see mineralogic evidence consistent with a paleolacustrine origin for deposits within these basins [*Stockstill et al.*, 2005]. Nevertheless, with a spatial resolution 1500–1800 times better than TES data [*Christensen et al.*, 2003], THEMIS allows us to search for potential evaporite deposits of a smaller scale than

was previously discernible. A terrestrial analog study by *Baldridge et al.* [2004] suggests that if evaporite minerals are widely exposed within the selected Martian study areas, they should be detectable at THEMIS spatial and spectral resolutions, but TES may have insufficient spatial resolution.

2. Methods

2.1. Data Compilation

[17] Both data sets were projected in the simple cylindrical system; since TES and THEMIS use different coordinates systems, the TES data was shifted to match the THEMIS coordinate system. THEMIS data for each basin were collected for images acquired prior to 1600 local solar time (LST). Scenes acquired later in the day were not used because of the inferior signal-to-noise ratios associated with cooler surface temperatures. Using custom software we wrote for use with ITT Industries' ENVI remote sensing package, geo-referenced and projected THEMIS multispectral radiance data were assembled into an image cube. A data mask band was created to filter pixels with incomplete data around the border of each scene. A maximum brightness temperature (T_b) image was calculated using a one-sided fit to the Planck function convolved to the THEMIS band passes. The T_b image was then evaluated to ensure that sufficient surface temperatures were present. THEMIS emissivity data are not considered trustworthy for surfaces below ~240 K [*Bandfield et al.*, 2004]; therefore, if most pixels (>50%) in the brightness temperature image were below 240 K, the radiance data were not processed further.

[18] TES spectra for this study include only those from nadir-pointing, daytime observations with TES orbit numbers (OCK) 1683–7000 and are further constrained to exclude data at risk for increased noise due to motion of the spacecraft's solar panel and high-gain antenna (HGA) and errors resulting from major phase inversions. The spectra for a given target area were assembled into a hyperspectral image cube also using custom software we have written for ENVI. For each hyperspectral image cube, an ancillary data cube was also constructed, which contains data planes for the latitudes, longitudes, TES temperatures, and TES albedo of every pixel, as well as observational data such as the TES OCK and ICK numbers. The THEMIS-derived regions of interest (ROIs) were overlain on the TES emissivity data, and mean TES emissivity spectra for each region were collected. As in *Stockstill et al.* [2005], the TES data we used were from individual TES spectra (not averaged into latitude/longitude bins a priori).

2.2. THEMIS Atmospheric Correction and Conversion to Surface Emissivity

[19] The spectral contribution from the atmosphere in THEMIS data includes both an additive term (atmospheric emission) and a multiplicative term (atmospheric attenuation of surface radiance) [*Bandfield et al.*, 2004].

2.2.1. Constant Radiance Offset (Additive) Correction and Conversion to Emissivity

[20] Atmospheric emissions are removed using the constant radiance offset removal algorithm of *Bandfield et al.* [2004]. This algorithm uses a geologic feature that can be assumed (through photogeologic arguments) to have fairly homogeneous emissivity spectrum but a wide range of temperatures (e.g., an impact crater that has both sunlit and shadowed crater walls). The algorithm calculates the offset value required for each band to produce a single emissivity spectrum for that geologic feature and applies the calculated radiance offsets to all pixels within the image. The corrected radiance data were then converted to emissivity by finding the highest brightness temperature from bands 3 to 9 (~1265–670 cm^{-1} or 7.9–12.6 μm) and dividing by the Planck function that corresponds to that brightness temperature [*Gillespie*, 1985; *Realmuto*, 1990], convolved to the THEMIS band passes. As a final step in creating the multispectral emissivity cube, bands 1 and 2 were co-added to enhance the signal at their shared wavelength. Co-adding these bands improves the signal-to-noise ratio, consequently reducing the emissivity difference required for reliable detection to >0.02 [*Christensen et al.*, 2004b].

2.2.2. Removal of Atmospheric Absorptions From Spectra (Multiplicative Correction)

[21] At this stage, THEMIS derived emissivity data contain spectral contributions from both the atmosphere and the surface in varying proportions. THEMIS data do not contain enough bands to use linear deconvolution to remove atmospheric spectral contributions, as is routinely done with TES [*Smith et al.*, 2000; *Bandfield et al.*, 2000a]. To determine the multiplicative correction required to remove the atmospheric spectral contribution in bands 3–9, a spectrally homogeneous region within the THEMIS data was identified and a mean THEMIS emissivity spectrum collected. This mean spectrum was compared to a mean TES surface emissivity for the same region and the multiplicative correction factor for THEMIS bands 3–9 was calculated [*Bandfield et al.*, 2004]. This correction factor was applied to each pixel within the image to produce a THEMIS surface emissivity image.

[22] The surface emissivity for bands 1 and 2 (~1472 cm^{-1} or ~6.8 μm) cannot be derived by this same technique because the TES atmospheric and surface end-members used in deconvolution do not extend beyond 1301 cm^{-1} (~7.7 μm), as shown in Figure 2. Data at higher wave numbers are excluded due to increased noise and contributions from water vapor at wave numbers >1350 cm^{-1} (>7.4 μm) [*Bandfield et al.*, 2000a; *Smith et al.*, 2000]. Instead, we have plotted raw (with atmosphere) THEMIS emissivity values for bands 1 and 2 for each ROI. Although carbonates have a strong absorption at these high wave numbers [*Lane and Christensen*, 1997], both water vapor and fine particulates may also cause reduced emissivity in THEMIS bands 1 and 2 precluding identification of the cause of an absorption in these bands. Instead, TES data was used to evaluate for the presence of these components, as described later in section 2.4.

2.3. Image Enhancement and Identification of Surface Spectral Units

[23] At this point, the emissivity data were evaluated to determine if sufficient spectral variation was present to warrant further analysis. To distill the large amount of data contained within a single THEMIS multispectral emissivity image, a technique based on principal component (PC) analysis was used. The PC-based application used for this study was a forward Minimum Noise Fraction (MNF) rotation in ENVI [*Green et al.*, 1988], producing an 8-band MNF image cube and associated eigenvalues. The result of

Table 1. Physiographic Information and THEMIS Scene Numbers for Basins Presented in This Paper

Crater Name[a]	C&G [1999] List Number[b]	Crater Center		Rim Diam., km	Depth, km	THEMIS Scene Number	Eigenvalues Associated With 8 MNF Bands Used to Determine How Much Real Variation Exists							
		°S	°E				b1	b2	b3	b4	b5	b6	b7	b8
Gusev	135	14.5	175.5	160	2.0	I01605002	14.0	7.8	6.3	5.2	4.9	4.8	4.6	0.0
						I01243001	19.7	7.3	7.0	5.7	5.3	5.0	4.9	0.0
						I00881002	34.8	10.6	9.6	6.1	5.3	5.2	5.1	0.0
						I00856001	23.3	11.4	10.7	7.6	6.2	5.9	5.5	0.0
Gale	85	5.4	137.8	142	2.2	I01131009	69.2	20.5	8.6	5.8	5.0	4.9	4.6	0.0
						I01469001	75.0	36.2	7.4	5.5	4.7	4.5	4.5	0.0
						I01855008	110.8	34.1	9.1	7.5	6.0	5.5	5.2	0.0
						I01494001	95.7	43.1	10.2	8.0	5.7	4.9	4.8	0.0

[a]Official name of crater.
[b]C & G [1999] refers to the *Cabrol and Grin* [1999] paper.

the MNF rotation was evaluated to determine the amount of spectral variability present in three ways. First, the eigenvalue plot was examined to determine how many MNF bands contained real spectral variation. Bands with large eigenvalues contain data; where the eigenvalue plot levels off, the bands contain noise. For example, for THEMIS scene I01855008 in Gale Crater, the first 2–3 bands have values above the background level; the remaining bands level off with an eigenvalue of ~6 and would be discarded (Table 1 and Figure 3a). Secondly, each band of the 8-band MNF image cube was evaluated as a gray scale images to identify which bands contained real surface spectral variation and which bands appeared to contained noise. Bands the displayed spatially contiguous patterns were considered to contain real spectral variation; bands that displayed random patterns (resembling static on television) were considered to contain noise (Figure 3b). Finally, the 8-band MNF image file was evaluated as 3-band color images in multiple MNF band combinations to evaluate the variability in the scene on the basis of how many colors were present in the 3-band image. If insufficient spectral variation was present within the scene (e.g., if no spatially contiguous colors appeared in the 3-band image of the first three MNF bands) no further analysis of that THEMIS image was pursued.

[24] We used decorrelation stretch (DCS) to enhance the spectral variation within a selected subset of three spectral emissivity bands [*Gillespie et al.*, 1986]. Decorrelation stretches are typically applied to highly correlated data (i.e., thermal radiance data) to highlight spectral differences rather than differences related to temperature. Using a DCS with emissivity data is essentially applying a contrast stretch to the emissivity data, which enhances spectral variations of three specified bands within the image. This produces a mosaic that displays basin-scale units in the same color across multiple THEMIS images; these same units may or may not display contiguous colors in the MNF mosaic. The DCS of emissivity bands 5, 7 and 8 is useful for enhancement of spectral variation related to two previously defined TES surface end-members, Surface Types 1 and 2 (J. Bandfield, personal communication, 2005). Using both MNF and DCS color composite images permitted identification of more spectral units (MNF) as well as assessment of the extent of these spectral units that spanned several THEMIS images (DCS). Additional band combinations used include the DCS of emissivity bands 6, 4 and 2, which would be useful for enhancement of spectral variation related to carbonates. However, due to the poor SNR in bands 1 and 2, these images appeared noisier, did not reveal any additional surface spectral units and will not be presented here.

2.4. Collection and Evaluation of Mean TES and THEMIS Spectra of Surface Spectral Units

[25] Next, ROIs were defined using the MNF and DCS images by outlining areas of contiguous colors within the image. (Note: Some ROIs corresponded to surface units defined in previous studies, in which case a similar naming convention was employed.) When all surface spectral units within the crater were defined, mean THEMIS emissivity spectra were calculated for all ROIs. These spectra were compared to the TES surface spectral end-members (Surface Types 1 and 2, hematite and surface dust) convolved to THEMIS band passes [*Bandfield et al.*, 2000b*; Bandfield and Smith*, 2003]. However, because THEMIS emissivity is restricted to 8 bands, its utility as a mineral/rock identifier is limited. Therefore evaluation of THEMIS spectra were used in concert with TES spectra of the same ROIs, where TES data coverage was available.

[26] The THEMIS-derived ROIs were overlain on the TES emissivity data, and mean TES emissivity spectra for each region were calculated. Because the surface may have changed between the time TES and THEMIS data were acquired, care was taken to sample the same surface spectral unit within the TES data.

[27] Mean TES ROI spectra were then evaluated using the dust cover index (DCI) of *Ruff and Christensen* [2002], which is sensitive to accumulations of dust on the order of a few tens of microns. Albedo measurements have a skin depth on the order of a few microns, whereas thermal inertia penetrates to an order of several cm [*Pelkey and Jakosky*, 2002]. Therefore the dust layer thickness derived from the DCI samples a skin depth that is intermediate between the skin depths sampled by albedo (i.e., optical thickness) and that sampled by thermal inertia (i.e., thermal thickness). Surfaces that have a dust layer that are thick enough to obscure spectral signature will return a DCI value of $\leq$0.940 and are referred to as dust covered. The spectra of dust-covered surfaces so-defined contain nothing but the same spectral signature of dust seen in all dusty regions of the planet. Because these spectra revealed nothing about the underlying surface composition, they were of no value to this study and were discarded. Surfaces that are essentially dust free (no dust to obscure the spectral signature) return a DCI value of $\geq$0.962 and are referred to as dust free [*Ruff and Christensen*, 2002]. In addition, the spectral signature

of the surface may be only partially obscured by dust, in which case it is referred to as intermediate [*Ruff and Christensen*, 2002]. The dust layer can be thought of as spectrally thick for dust covered surfaces, spectrally intermediate for intermediate surfaces, and spectrally thin for dust free surfaces. The DCI value is important for evaluating THEMIS spectra with apparent absorptions in band 1 and 2 emissivity, since particle size effects can cause reduced emissivity in these bands.

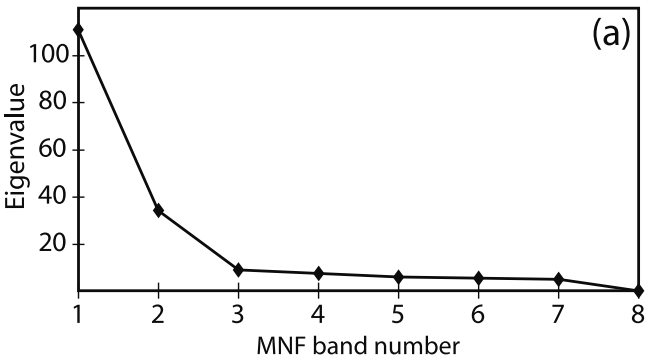

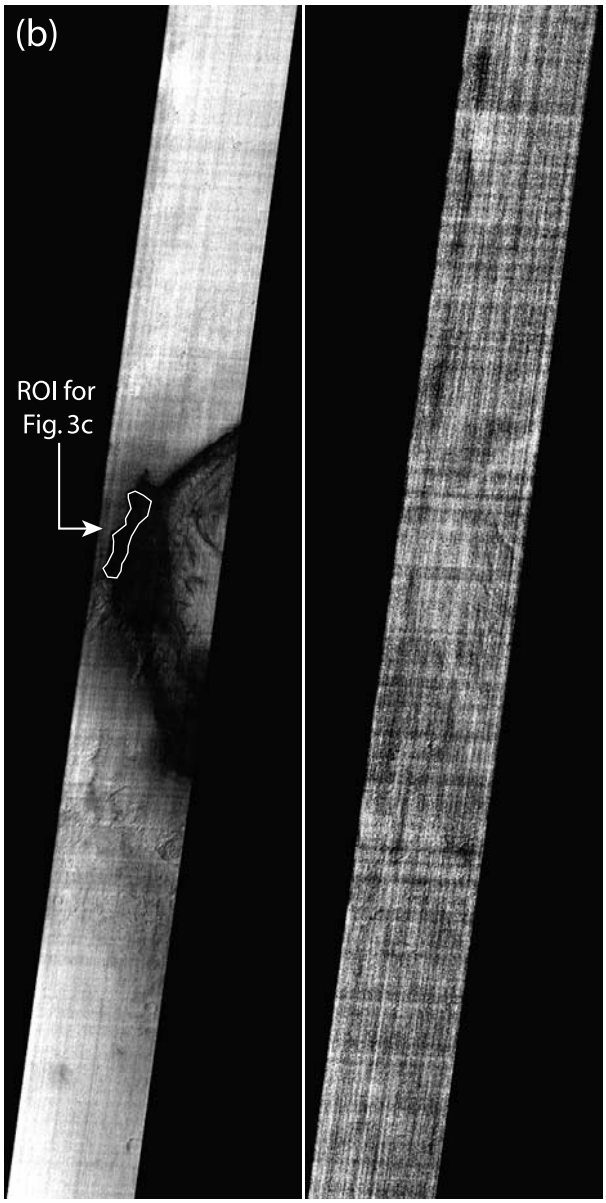

[28] Next, the mean TES ROI spectra were evaluated using the linear deconvolution technique of *Smith et al.* [2000] and *Bandfield et al.* [2000a]. The deconvolution technique fits the measured TES apparent emissivity spectrum in a linear least squares sense using both atmospheric spectral shapes and surface spectral shapes simultaneously. This strategy is based on the empirical finding that atmospheric spectral components may be treated as linearly mixed end-members in emissivity-space [*Feely and Christensen*, 1999; *Gillespie*, 1992; *Ramsey and Christensen*, 1998; *Smith et al.*, 2000; *Thomson and Salisbury*, 1993]. The surface spectral end-members consisted of the TES Surface Types 1 and 2, the hematite end-member [*Bandfield et al.*, 2000a] and an average high albedo surface end-member [*Bandfield and Smith*, 2003]. Atmospheric spectral end-members included a high CO_2 dust end-member, a low CO_2 dust end-member, and two water-ice cloud end-members. Although atmospheric dust is distributed fairly homogeneously in the Martian atmosphere, water ice clouds can be variable in both distribution and their affect on TES data. Regardless, linear deconvolution provides a powerful tool for estimating the abundances of the atmospheric end-members [*Bandfield et al.*, 2000a]. These comprise the eight previously identified global TES end-members that were used in the *Stockstill et al.* [2005] study, allowing for direct comparison to previous results.

[29] Finally, the mean TES ROI spectra were then evaluated using the spectral ratio technique and carbonate indices of *Stockstill et al.* [2005]. The spectral ratio technique uses the ratio of the measured ROI spectrum to the deconvolution modeled spectrum in an effort to highlight residual surface spectral features that are not well modeled by the eight TES end-members. As illustrated in Figure 3c, where the modeled emissivity deviates from the measured emissivity, the spectral ratio value deviates from unity. This technique relies on the fact that the eight TES end-members are dominated by relatively broad and deep features that would not mask the narrower features of carbonates or other minerals. At 270 K, the NE$\Delta\varepsilon$ for TES is 0.002 [*Christensen et al.*, 1992], so the spectral ratio value must vary from unity by ±0.002 to be considered above the noise level. Thus, where the ratio deviates from unity (>±0.002)

Figure 3. Example of how real spectral variation is evaluated for a given THEMIS scene, in this case scene I01855008 covering Gale Crater. (a) Example of an eigenvalue plot used to assess how much spectral variation is present within a scene. (b) Example of MNF bands that display real spectral variation (left) and noise (right). The width of the THEMIS strip is ~32 km across. The region of interest used to demonstrate the spectral ratio method in Figure 3c is outlined in white on the MNF band image displaying real spectral variation (left). (c) Plot of the measured (black) and modeled (gray) TES spectrum for the region of interest outlined in Figure 3b. The spectral ratio (dashed line) of the measured spectrum over modeled spectrum is illustrated above the spectra and varies around unity.

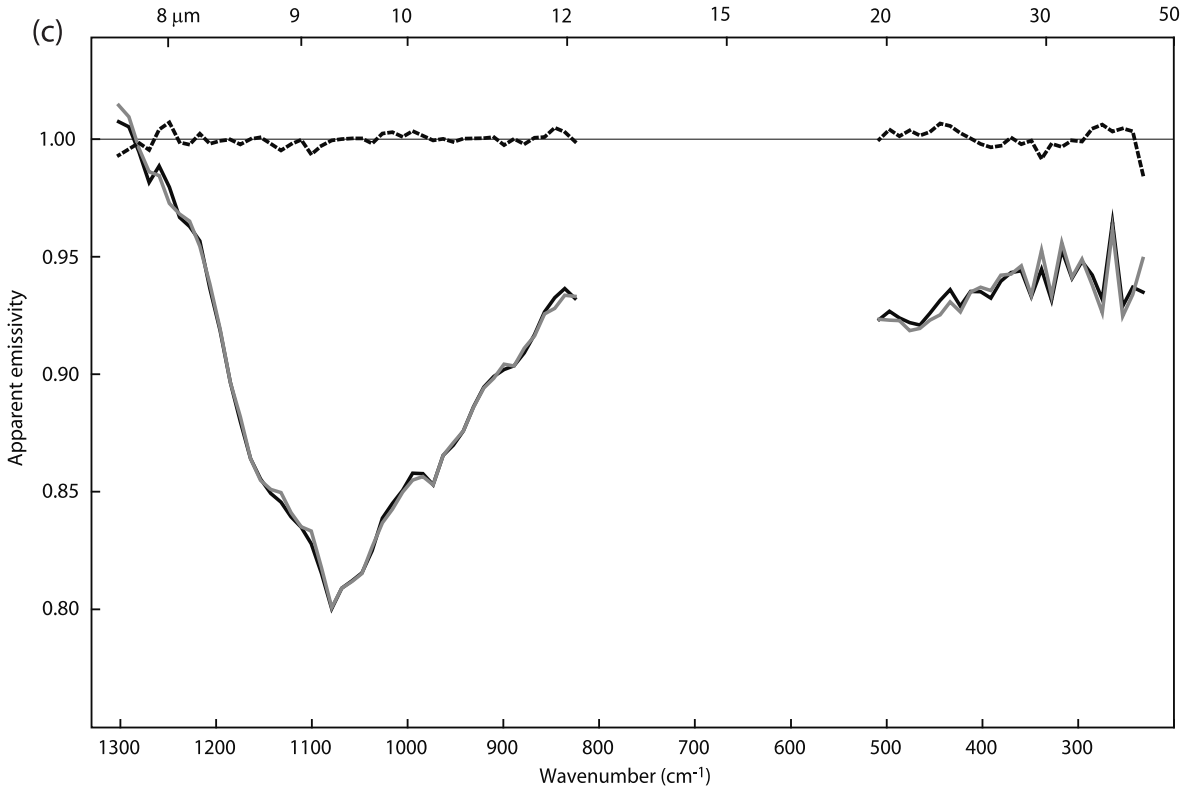

Figure 3. (continued)

for 4 or more consecutive bands (based on observed minimum absorption widths for igneous and evaporite minerals), there may be an absorption not well modeled by the deconvolution routine, or a residual absorption feature. For these cases, we noted both the location and the width of the remnant absorption and searched for a mineral or atmospheric end-member (e.g., CO_2 vapor or water vapor) not used in linear deconvolution that might cause in the observed remnant absorption.

[30] To further address the identification of carbonates in the mean TES ROI spectra, we used spectral indices sensitive to carbonates, to look for the presence of calcite, magnesite and siderite features [*Stockstill et al.*, 2005]. Similar in concept to the hematite index of *Christensen et al.* [2000a], the dust cover index of *Ruff and Christensen* [2002] and the bound water index of *Ruff* [2004], our carbonate indices were tuned to be sensitive to the carbonate absorption features near 890 cm^{-1} and 350 cm^{-1} (11 and 29 μm). The exact positions of the minima of carbonate spectral absorptions vary with composition and this variation is sufficient to distinguish between them at TES (10-cm^{-1}) spectral sampling [*Lane and Christensen*, 1997]. Although spectra of other minerals (e.g., silicates) may also have absorptions near these same wave numbers, carbonate spectra are unique in that the absorption feature near 350 cm^{-1} is between 1.75 and 2.63 times deeper than the 890-cm^{-1} absorption feature. Therefore the depths of these two absorptions relative to each other may be used to distinguish carbonate spectra from the spectra of other mineral classes. Decreasing particle size does not have a significant effect on the relative depth of these two absorption features, except for the smallest particle sizes (e.g., for 90–125 μm size range and smaller) [*Stockstill et al.*, 2005]. In spectral mixtures, the lower detection limits vary depending on which carbonate species is involved and whether that carbonate is mixed with bright or dark materials; lower detection limits for the carbonate indices range from 18–43% for the calcite index, 12–45% for magnesite index and 20–53% for siderite index [*Stockstill et al.*, 2005].

3. Results

[31] The results for Gusev and Gale craters are presented here. Table 1 displays physiographic information for these craters, lists the THEMIS scenes used in this study and eigenvalues associated with the MNF of each THEMIS scene.

3.1. Gusev Crater (14.5°S, 175.5°E)

[32] The regions of interest for Gusev Crater are displayed on a radiance offset corrected THEMIS daytime T_b mosaic in Figure 4a. The most distinct spectral unit in both PCA images (Figure 4b) is that associated with the previously identified low-albedo (LA) features [e.g., *Milam et al.*, 2003] and we retain that naming convention. However, these features were identified because they are spectrally distinct from the crater floor, the second surface unit (Figures 4a and 4b).

[33] The mean TES spectra of the THEMIS-determined ROIs in Gusev Crater were evaluated using the DCI of *Ruff and Christensen* [2002]. All regions were seen to exhibit some degree of surface dust cover according to the DCI (Table 2). The DCI values for the LA features indicate only intermediate dust cover (Table 2), whereas the DCI values of the crater floor ROI spectra from three different THEMIS

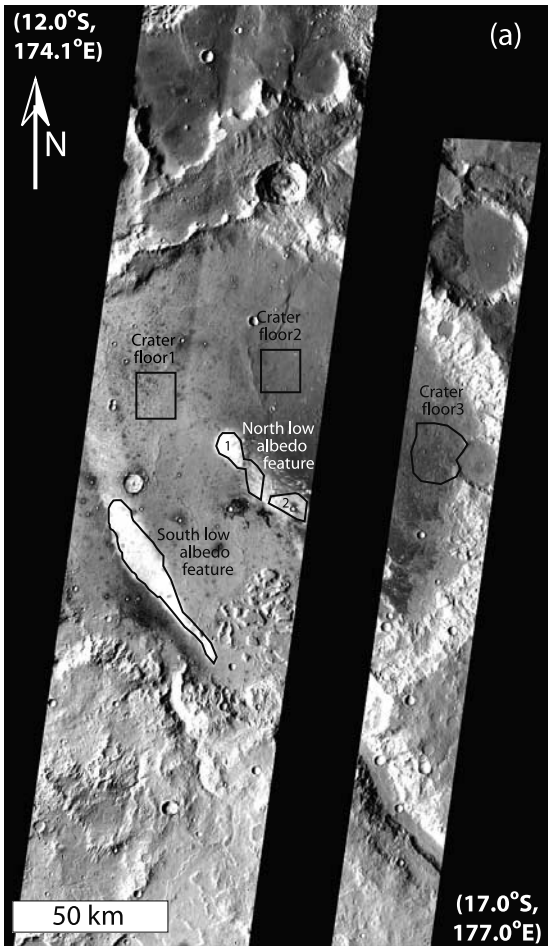

Figure 4. (a) Mosaic of four THEMIS corrected T_b images of Gusev crater showing the location of regions of interest discussed in the text. In constructing the T_b mosaics, individual images were normalized to each other to erase image seams within the mosaic. Note that ROIs were defined on the basis of the spectral variation (i.e., using the MNF and/or DCS images), so ROI boundaries may not correspond to thermophysical units observable within this T_b mosaic. From left to right, THEMIS stamps are I01605002, I01243001, I00881002 and I00856001. (b) Mosaic of decorrelation stretched images for the four THEMIS stamps covering Gusev Crater, overlain on a MOLA-derived shaded relief map. The decorrelation stretch used bands 5, 8, 7 assigned to R, G, B, respectively. (c) Mosaic of MNF images for the four THEMIS scenes covering Gusev Crater, overlain on a MOLA-derived shaded relief map. Each individual MNF image contains some combination of the first three MNF bands, but the order in which they are displayed into RGB varies. This was done in order to display similar units in similar colors (e.g., the low-albedo deposits in red), providing a more contiguous image. From left to right, the MNF band orders assigned to R,G,B are as follows: 3,1,2; 1,2,3; 2,1,3; and 1,2,3. Color variations that appear related to shading result from the shaded relief map only; emissivity data and subsequent data products do not display this shading effect.

images indicate that the crater floor is an intermediate to dust covered surface.

[34] TES linear deconvolution results for Gusev Crater (Table 2) are consistent with the DCI with respect to their use of the surface dust end-member, except for two ROIs. The deconvolution models of the south LA feature and Crater floor 1, which have DCI values that are intermediate (0.943) but approaching the dust cover threshold (0.940), do not include surface dust or any other surface end-members (Surface Types 1 and 2, or Hematite) in amounts exceeding the lower detection limits of 10–15% for this method [*Bandfield et al.*, 2000a]; instead, the models only include low CO_2 atmospheric dust in significant amounts (Table 2). Dust opacity measurements for these TES data were greater than 0.2, indicating that the atmosphere is completely obscuring the spectral signature of the surface and that no useful information is being garnered from the surface. The remaining six models include at least one surface end-member and will be discussed in terms of those surface components only. All remaining ROI models include the surface dust end-member, consistent with their DCI values. In general, the crater floor is well modeled by surface dust, possibly mixed with some Surface Type 2 materials. The north low-albedo feature appears to be well modeled by surface dust, with some Surface Type 2 materials exposed in some portions of this unit.

[35] The variation displayed by the measured-to-modeled spectral ratios for these ROIs appears to be related to the dusty nature of these spectra and to spectral contributions of CO_2 vapor and water vapor not used during linear deconvolution (Figure 5). Specifically, the concave-down shape of ratio values at the highest wave numbers is typically observed in spectra that have a spectrally thick layer of surface dust [*Stockstill et al.*, 2005]. This remnant absorption is present in all Gusev ROI spectral ratios. In addition, the erratic and divergent ratio values at the lowest wave numbers are similar in appearance and location to absorption from water vapor [*Smith*, 2002]. This remnant absorption is very strong in the spectral ratio of crater floor 1 and the south LA feature. Finally, the spectral ratio of crater floor 1 has a poor fit in the ~1100- to ~1225-cm^{-1} (9- to 8-μm) range due to remnant absorption from CO_2 vapor. Therefore the remnant absorptions observed in the spectral ratio plots for the Gusev ROIs are due to atmospheric water vapor and/or dust. These spectral ratios do not contain remnant absorptions due to a unique mineralogy that linear deconvolution using the eight TES end-members failed to model. Furthermore, application of the carbonate indices method did not indicate the signature of carbonates for any region defined for this basin.

[36] Mean THEMIS surface emissivity spectra for the Gusev ROIs are displayed in Figure 6. The emissivity spectra of the LA features display the most spectral contrast of any ROI spectra from this crater (Figure 6). Unfortunately, these spectra do not display sufficient spectral contrast to distinguish between Surface Types 1 and 2 (Figure 2) and these emissivity spectra could be interpreted as either Surface Type 1 or 2 mixed with dust. Mean THEMIS surface emissivity spectra for the crater floor ROIs display less spectral contrast, consistent with a relatively dustier surface (Figure 6). Spectra for crater floor 2 and 3 strongly resemble the surface dust spectrum (Figure 2). The crater floor 1 spectrum displays a minimum in band 5 (Figure 6) similar to the Surface Type 2 spectrum (Figure 2), but exhibits less

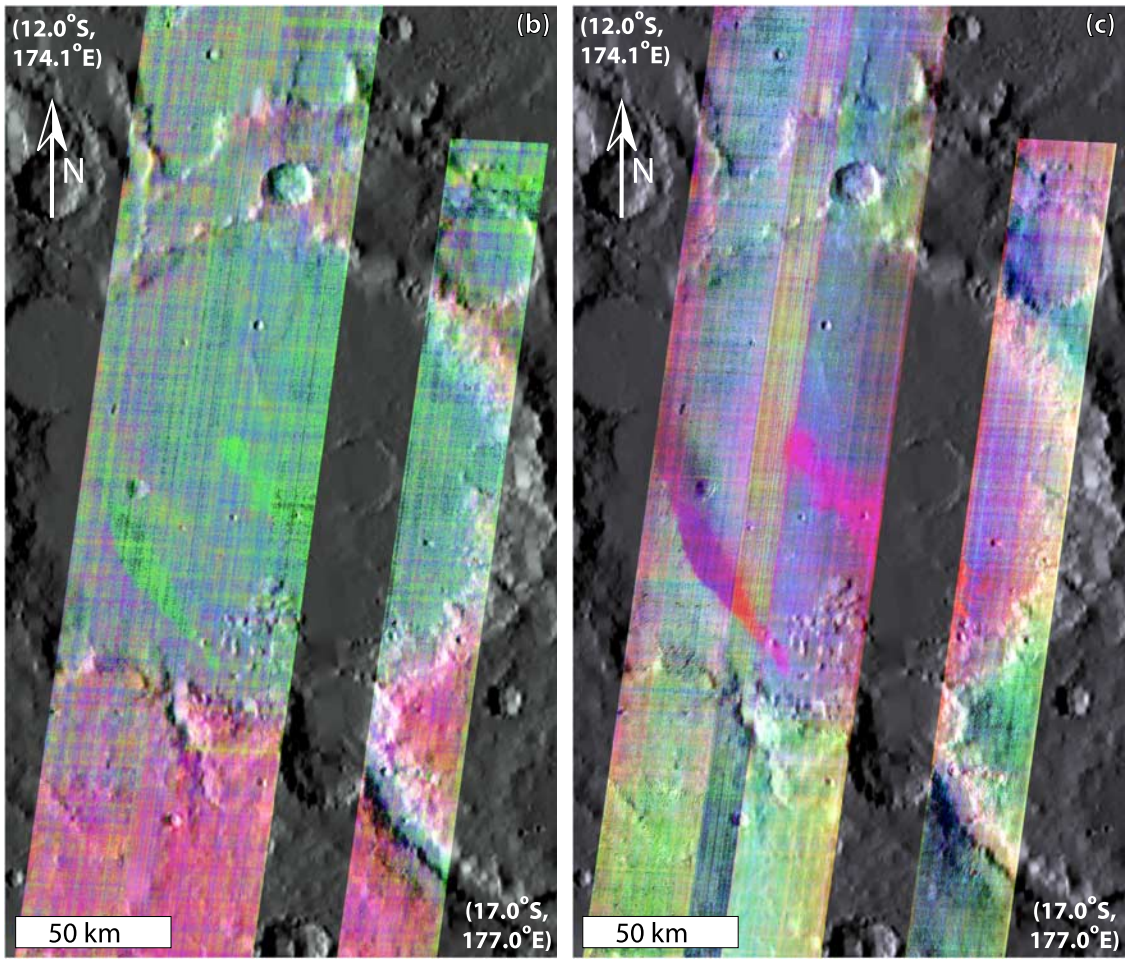

Figure 4. (continued)

spectral contrast. Therefore this spectrum may represent a mix of Surface Type 2 and dust.

3.2. Gale Crater (5.5°S, 137.8°E)

[37] The regions of interest for Gale Crater are displayed on a corrected THEMIS T_b mosaic in Figure 7a. Numerous spectrally distinct ROIs have been defined within the floor of Gale Crater and are displayed on the T_b mosaic of Gale Crater (Figure 7a). The most evident unit wraps around the crater's central mound in the NW and NE and is present in the southern crater floor in both the DCS mosaic (Figure 7b) and in the MNF mosaic (Figure 7c). This unit corresponds to the low albedo (relative to the surrounding crater floor) identified in TES data by *Pelkey et al.* [2004] and we will refer to these as low-albedo units (although they were identified due to their spectral variability). We have defined

Table 2. Results From Deconvolution of TES Emissivity Data, Where Available, for Gusev Crater Using Only the TES End-Members[a]

	Gusev Crater Floor			South Low-Albedo Feature	North Low-Albedo Feature	
	Floor 1	Floor 2	Floor 3		Feature 1	Feature 2
Surface Type 1	0.0	0.0	0.0	6.0	0.0	0.0
Surface Type 2	0.0	0.0	**14.0**	9.0	**25.0**	0.0
Hematite	0.0	0.0	0.0	0.0	0.0	0.0
Surface dust	0.0	**30.5**	**36.5**	0.0	**22.0**	**35.5**
Dust Low-CO_2	**97.0**	**62.5**	**27.5**	**82.0**	**18.5**	**63.5**
Dust High-CO_2	0.0	4.5	**20.0**	0.0	**29.0**	0.0
H_2O Ice $Cloud_1$	3.0	0.0	0.0	0.0	0.0	0.0
H_2O Ice $Cloud_2$	0.0	3.0	3.0	2.5	6.5	1.5
Sum	100.0	100.5	101.0	99.5	101.0	100.5
Spectral RMS	0.01027	0.00294	0.00292	0.00449	0.00325	0.00470
DCI value	0.943	0.937	0.935	0.943	0.941	0.943
Interpretation	intermediate	dust covered	dust covered	intermediate	intermediate	intermediate
THEMIS interpretation	ST2 + Dust	Dust	Dust	ST1 or ST2? + Dust	ST1 or ST2? + Dust	ST1 or ST2? + Dust

[a]End member values have been rounded to the nearest 0.5%. Percentages in bold indicate end-members used in significant amounts (>10–15%; see text). DCI value and interpretation are based on *Ruff and Christensen* [2002]. For THEMIS interpretation, ST1 is Surface Type 1; ST2 is Surface Type 2; Dust is surface dust.

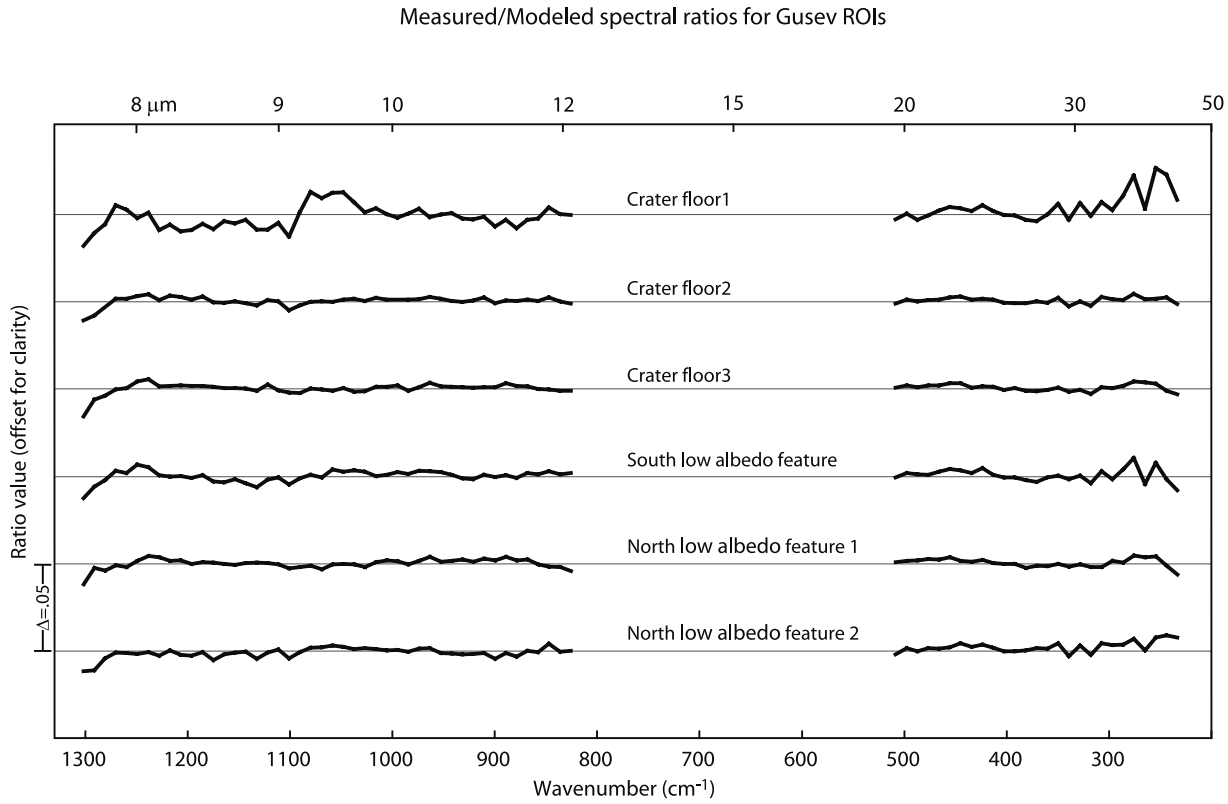

Figure 5. Measured-over-modeled spectral ratios from TES data of the Gusev ROIs, offset 0.05 for clarity.

three ROIs on the THEMIS mosaic that have overlapping TES coverage to sample this low-albedo material. In addition, a "smooth" crater floor ROI just SSW of the mound and a central crater floor ROI have been defined within the crater floor. These units do not appear to be distinct in the DCS mosaic (Figure 7b), although they do appear to be a more intense shade of green than their surroundings in the MNF mosaic (Figure 7c). Furthermore, the mound is spectrally distinct from the crater floor, with the central portion of the mound appearing to be distinct from the flanks on either side in both the DCS and MNF images. We have defined four ROIs on the mound to collect spectra from different portions of the mound.

[38] When the mean ROI TES spectra of Gale Crater were evaluated using the DCI [*Ruff and Christensen*, 2002], the ROI spectra varied from dust covered (the western portion of the mound) to dust-free (the crater floor), as shown in Table 3. The dustiest region is the mound, although the dust layer thickness varies from dust covered in the west to intermediate dust cover for the central mound (Table 3). The crater floor appears to be relatively dust-free (Table 3).

[39] Linear deconvolution results for Gale Crater, also displayed in Table 3, are relatively consistent with the DCI in regard to their use of the surface dust end-member. In terms of the surface components, the low-albedo materials and the central crater floor are well modeled by a combination of Surface Types 1 and 2 materials and are distinct from the smooth unit, which is well modeled using only Surface Type 1 materials. The surface component of the deconvolution results for the western mound unit includes only surface dust component in significant amounts, among the largest amount of surface dust of any ROI, which is consistent with it also having the lowest (dustiest) DCI value. The central mound and mound layers do not use significant amounts of surface dust, consistent with their intermediate DCI values. The surface components for the deconvolution of the central mound unit included a mix of Surface Types 1 and 2 materials, whereas the mound layers unit only included Surface Type 2 material.

[40] The variation displayed by the measured-to-modeled spectral ratios for the Gale ROIs appears to be related to spectral contributions for CO_2 vapor and water vapor not used during linear deconvolution (Figure 8). The spectral contribution of water vapor at low wave numbers is apparent in the top four spectral ratios, especially in the smooth crater floor ratio. In addition, a poor fit due CO_2 vapor at high wave numbers ($\sim$1100–1225 cm^{-1} or 9–8 μm range) appears in most ROIs, but is especially apparent in the smooth crater floor and the mound layers ratios. Therefore the remnant absorptions observed in the Gale ROIs are due to atmospheric CO_2 vapor and water vapor. These spectral ratios do not contain remnant absorptions due to a mineral or minerals that were not provided for linear deconvolution. In addition, application of the carbonate indices method did not indicate the signature of carbonates for any region defined for this basin.

[41] Mean THEMIS surface emissivity spectra for the Gale ROIs are displayed in Figure 9. The spectra of the crater floor and the low-albedo materials on the crater floor show a range of spectral shapes from the Smooth Crater floor to the W low-albedo material (Figure 9). The smooth

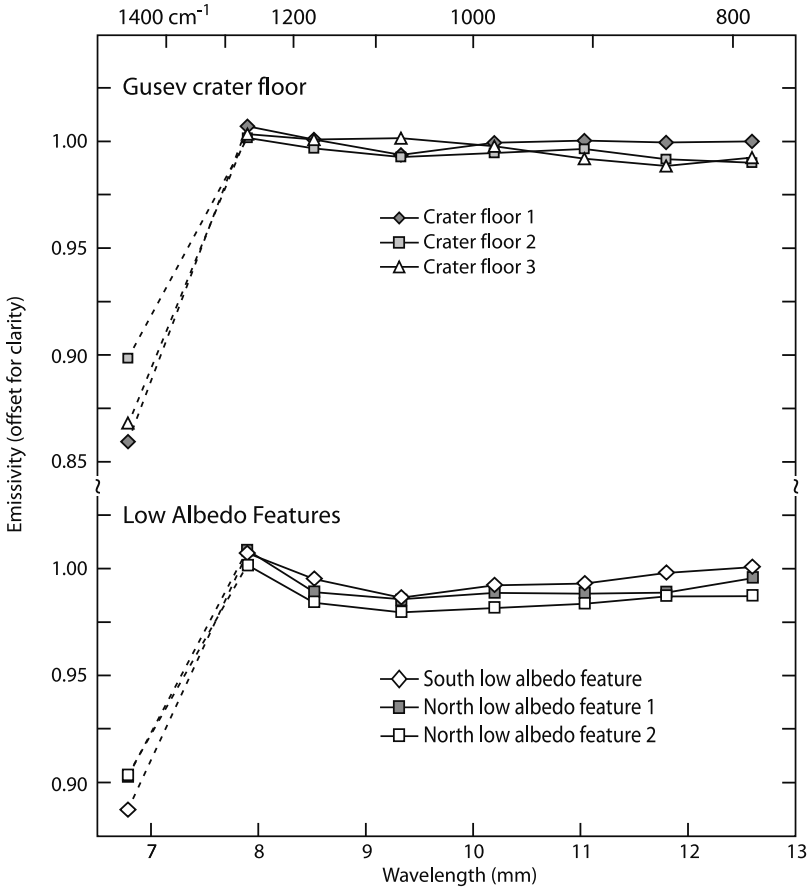

Figure 6. Mean THEMIS emissivity spectra for groups of ROIs defined for Gusev Crater. Note that the emissivity values displayed for bands 1 and 2 are apparent emissivity values, not true emissivity. Standard deviations for bands 3–9 are the height of the symbol or smaller. Standard deviations for bands 1 and 2 are twice the height of the symbol or smaller (with the exception of the Crater floor 1 ROI spectrum, whose standard deviation is 2.3 times the height of the symbol).

crater floor spectrum has a general minimum from bands 5–7, with the absolute minimum in band 6, similar in shape and spectral contrast to the Surface Type 1 spectrum. This is consistent with a relatively dust free basaltic surface. The remaining ROIs display a minimum in band 5–7, but with a general increase in emissivity from band 5 to 7 and no absolute minimum in band 6. This shape is most consistent with a mixture of Surface Types 1 and 2 (Figure 2). In addition, the decreasing spectral contrast may indicate increasing surface dust. The spectra of all mound units show less spectral contrast consistent with a dustier surface, with the eastern mound spectrum most resembling the surface dust end-member spectrum (Figure 2).

4. Discussion

4.1. Gusev Crater (14.5°S, 175.5°E)

[42] The DCI values of the LA features are consistent with either a surface with intermediate dust cover or a surface with more indurated particulate materials [*Ruff and Christensen*, 2002]. Fortunately, the Spirit Rover landed within one of the regions of low albedo in Gusev Crater and these low-albedo features are now believed to be zones that have had recent removal of some fine particulate material by dust devils [*Squyres et al.*, 2004]. Both thermal inertia measurements and albedo measurements in the area of the Spirit landing site are consistent with a surface dominated by duricrust to cemented soil-like materials or cohesionless sand and granules [*Bell et al.*, 2004; *Christensen et al.*, 2004a; *Squyres et al.*, 2004].

[43] *Martínez-Alonso et al.* [2005] identified the LA features as a surface that is a mixture of indurated material, coarse particles, and exposed rocks or bedrock that has a basaltic composition. Spirit rover analyses also showed that many rocks within Gusev Crater appear to be pristine basalts containing olivine [*Christensen et al.*, 2004a; *McSween et al.*, 2004; *Morris et al.*, 2004]. Furthermore, even the regolith shows only a slight decrease in basaltic mineralogy in trenches relative to the undisturbed surface regolith [*Wang et al.*, 2005], suggesting relatively little alteration of the rocks and regolith in this portion of Gusev Crater.

[44] Contrasting with other studies, linear deconvolution of the low-albedo features for this study included Surface Type 2, not Surface Type 1. Surface Type 2 has been interpreted as either an andesite [*Bandfield et al.*, 2000a; *Hamilton et al.*, 2001] or as partly weathered basalt [*Wyatt and McSween*, 2002; *Kraft et al.*, 2003; *Ruff*, 2004]. Neither interpretation is consistent with relatively unaltered basaltic terrain evidenced by Spirit Rover and the study of *Martínez-*

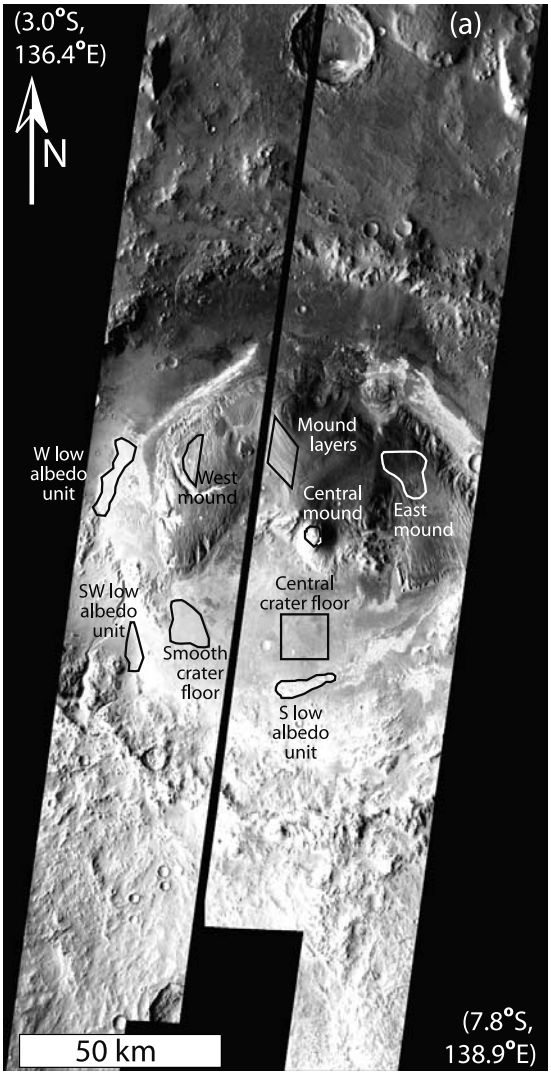

Figure 7. (a) Mosaic of four THEMIS corrected T_b images of Gale crater showing the location of regions of interest discussed in the text. The ROIs were defined on the basis of the spectral variation; therefore thermophysical units observed within this T_b mosaic may not correspond with any defined ROI boundaries. From left to right, THEMIS stamps are I01855008, I01494001, I01131009 and I01469001. (b) Mosaic of decorrelation stretched images for the four THEMIS stamps covering Gale Crater, overlain on a MOLA-derived shaded relief map. The decorrelation stretch used bands 5, 8, 7 respectively. (c) Mosaic of MNF images for the four THEMIS stamps covering Gale Crater, overlain on a MOLA-derived shaded relief map. Again, each individual MNF image contains some combination of the first three MNF bands, but the order in which they are displayed into RGB varies. This was done in order to display similar units in similar colors (e.g., the crater floor material that appears in green) and produce a more contiguous image. From left to right, the MNF band orders assigned to R,G,B are as follows: 1,3,2; 1,2,3; 1,2,3; and 2,1,3. Color variations that appear related to shading result from the shaded relief map only; emissivity data and subsequent data products do not display this shading effect.

Alonso et al. [2005]. TES linear deconvolution of Surface Type 1 materials mixed with sulfates [*Lane*, 2005] may result in the inclusion of Surface Type 2 materials instead when sulfates are not provided (M. Lane, personal communication, 2005). The regolith in Gusev Crater has been found to contain up to 16% sulfates [*Wang et al.*, 2005]. So we repeated the linear deconvolution using the eight TES end-members plus library spectra of bloedite and glauberite, two sulfate species previously identified on Mars [*Lane*, 2005] whose spectra were available to us. When these sulfates were provided, bloedite and glauberite were included in the models and only in small amounts (Table 4), well below their lower detection limit of 15% [*Christensen et al.*, 2001]. Furthermore, the spectral RMS would need to improve more than 0.0013 to exceed difference due to noise [*Christensen et al.*, 1992; V. Hamilton, personal communication, 2006]. However, including sulfate end-members does not improve the spectral RMS significantly for any model (Table 4) or drastically change the measured-to-modeled spectral ratio (Figure 10). This indicates that neither model (using only the eight TES end-members or using the eight TES end-members plus sulfates) provides a significantly better fit than the other. However, the inclusion of sulfates did eliminate the use of the Surface Type 2 end-member from some models and increase the amount of Surface Type 1 used to significant amounts (e.g., >10%) for these models (e.g., the south LA feature, Table 4). This illustrates that the results from linear deconvolution may vary when different end-member sets are provided. In any case, this model provides a better match to the surfaces observed at Gusev by the Spirit rover. Note that the models for the north LA feature are fairly unaffected by the inclusion of sulfates for modeling; however, these units also appear to be dustier than the south LA feature, because they use up to 37% surface dust end-member. Therefore it is possible that the surface composition of this area of the north LA feature was obscured by more dust at the time the TES data were acquired. Unfortunately, at the time that the THEMIS spectra were obtained, the low-albedo units had sufficient surface dust to reduce spectral contrast so that the subtle spectral differences between Surface Types 1 and 2 in THEMIS spectra (Figure 2) cannot be identified with certainty. Therefore the THEMIS spectra of the low-albedo units (Figure 6) have a spectral shape that resembles either Surface Type 1 or 2 spectrum mixed with dust.

[45] The study of *Martínez-Alonso et al.* [2005] mapped the rest of the crater floor as a variety of units, ranging from basalt to dust covered surfaces. The crater floor 1 ROI overlaps transitional materials with properties intermediate between that of the plains materials unit (surface dust) and the high thermal inertia units (basalt); the remaining crater floor ROIs overlap the plains materials unit [*Martínez-Alonso et al.*, 2005]. This is consistent with the DCI values derived in this study, ranging from intermediate for Crater floor 1 to dust covered for Crater floor 2 and 3 ROIs (Table 2). In the case of crater floor 1 ROI, the models included Surface Type 1 materials when sulfates were provided for TES linear deconvolution (Table 2); however, for the remaining crater floor ROIs, Surface Type 2 and surface dust were the only surface end-members used in significant amounts. In addition, the THEMIS spectra of Crater floor 1

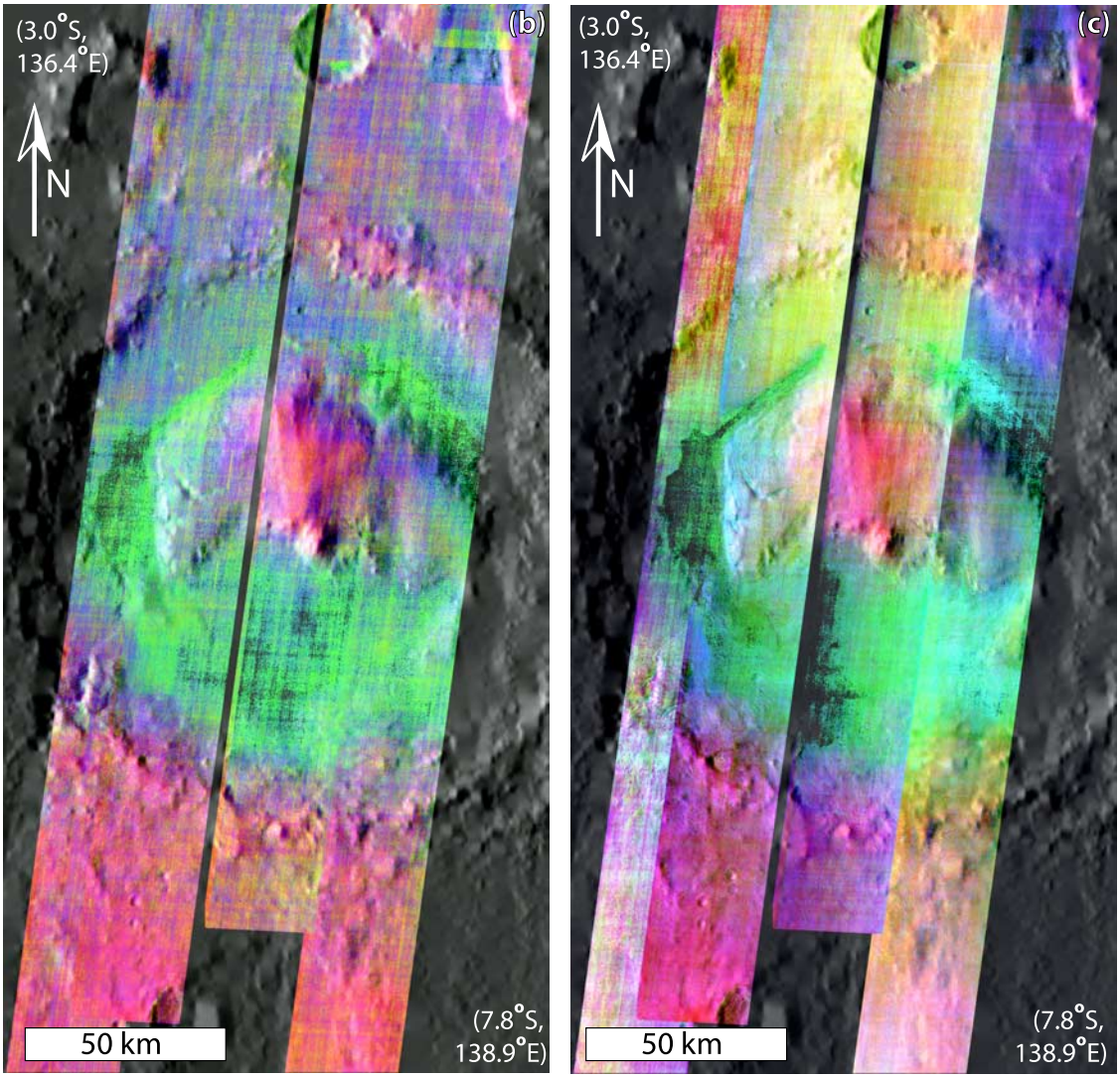

Figure 7. (continued)

Table 3. Results From Deconvolution of TES Emissivity Data, Where Available, for Gale Crater Using Only the TES End-Members[a]

	W Low-Albedo Material	SW Low-Albedo Material	S Low-Albedo Material	Smooth Crater Floor	Central Crater Floor	West Mound	Mound Layers	Central Mound	East Mound[b]
Surface Type 1	**11.5**	**41.5**	**35.5**	**33.5**	**31.0**	0.0	5.5	**12.0**	-
Surface Type 2	**13.5**	**13.5**	**24.0**	0.0	**26.0**	7.5	**11.5**	**15.0**	-
Hematite	0.0	0.0	0.0	0.5	0.0	0.0	0.0	1.5	-
Surface dust	0.0	0.0	0.0	0.0	0.0	**25.0**	0.0	5.0	-
Dust Low-CO_2	**68.5**	**31.0**	**26.5**	**63.0**	**28.0**	**30.5**	**73.5**	**29.0**	-
Dust High-CO_2	0.0	8.0	**11.0**	0.0	**11.5**	**21.5**	4.0	**28.5**	-
H_2O Ice $Cloud_1$	0.0	0.5	0.0	2.0	0.0	8.5	2.0	1.5	-
H_2O Ice $Cloud_2$	6.0	5.5	2.5	0.0	2.5	8.0	3.5	7.5	-
Sum	99.5	100.0	99.5	99.0	99.0	101.0	100.0	100.0	-
Spectral RMS	0.00323	0.00299	0.00366	0.00462	0.00330	0.00317	0.00470	0.00297	-
DCI value	0.960	0.967	0.967	0.963	0.966	0.929	0.944	0.954	-
Interpretation	intermediate	dust free	dust free	dust free	dust free	dust covered	intermediate	intermediate	-
THEMIS interpretation	ST1 + ST2 + Dust	ST1 + ST2	ST1 + ST2	ST1	ST1 + ST2	Dust	Dust	Dust	Dust

[a]End member values have been rounded to the nearest 0.5%. Percentages in bold indicate end-members used in significant amounts (>10–15%; see text). DCI value and interpretation are based on *Ruff and Christensen* [2002]. For THEMIS interpretation, ST1 is Surface Type 1; ST2 is Surface Type 2; Dust is surface dust.

[b]No TES coverage.

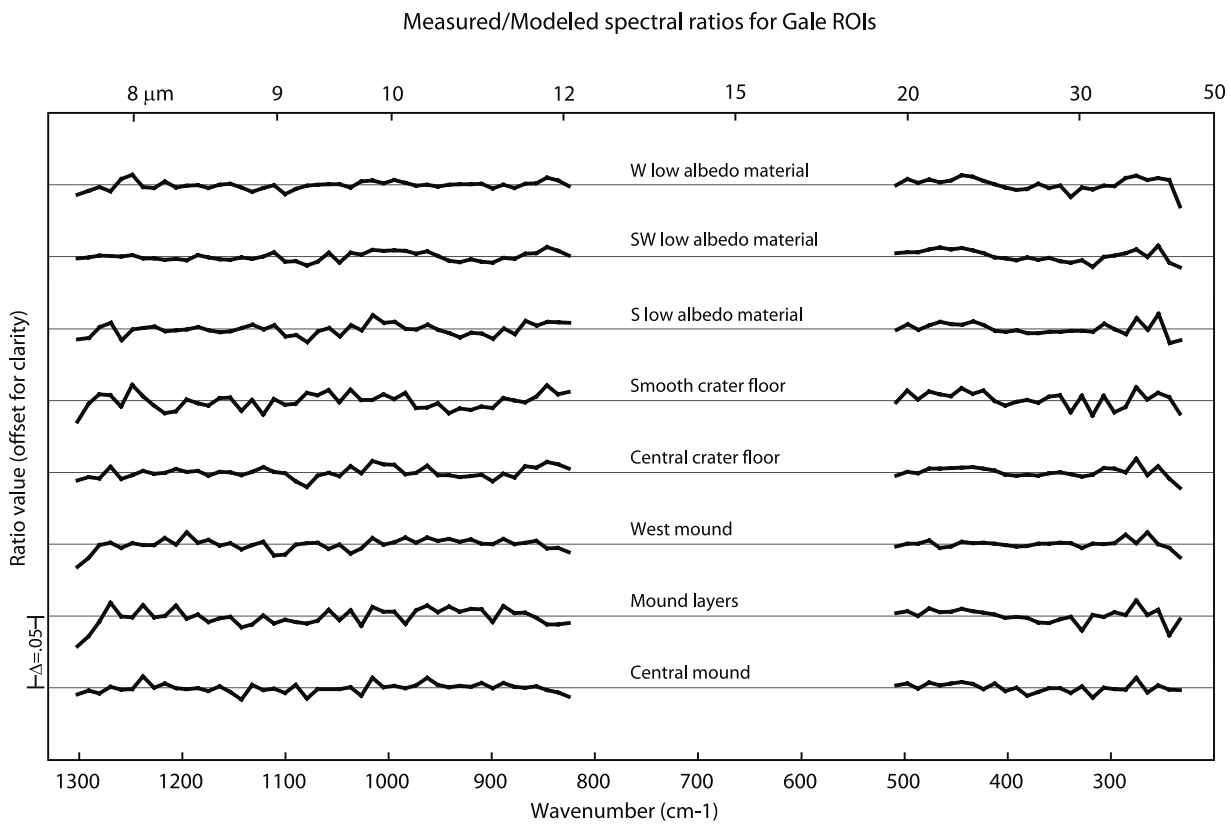

Figure 8. Measured-over-modeled spectral ratios from TES data of the Gale Crater ROIs, offset 0.05 for clarity.

ROI matches most closely to a mix of dust and some Surface Type 2.

4.2. Gale Crater (5.5°S, 137.8°E)

[46] The surface deposits at Gale Crater have less dust cover than the surfaces at Gusev Crater. The crater floor units have DCI values that indicate they are relatively dust-free surfaces, in agreement with previously published thermal inertia values for these units that suggest they range from lightly to extensively indurated materials with small amounts of dust [*Pelkey et al.*, 2004]. The deconvolution results of the crater floor units suggest they are composed of Surface Type 1 basalt mixed with some Surface Type 2 material. Mean THEMIS emissivity spectra of the crater floor units (Figure 9) resemble a range of spectral shapes, from Surface Type 1 to a mix of Surface Types 1 and 2 (Figure 2).

[47] Likewise, the low-albedo units within the floor of Gale Crater have DCI values that indicate relatively little dust cover, ranging from intermediate dust cover to dust-free. The W low-albedo materials are sand sheets mapped in the floor of Gale Crater by *Pelkey et al.* [2004]. Thermal inertia values from that study suggested that these materials consisted of coarse or lightly indurated sand that is at least a few cm in thickness [*Pelkey et al.*, 2004]. Like the rest of the crater floor, the deconvolution results for the low-albedo materials were consistent with a mix of Surface Types 1 and 2. In addition, THEMIS emissivity spectra for these units (Figure 9) are consistent with a mix of Surface Types 1 and 2 spectral shapes (Figure 2).

[48] The mound units correspond to areas from *Pelkey and Jakosky* [2002] where albedo and thermal inertia measurements indicated an optically thick but thermally thin layer of dust. Both the mound layers and the central mound unit have a DCI value that indicates only intermediate dust cover, whereas the W mound unit has a low DCI value that indicates a dust covered surface. The deconvolution results for the mound layers and the central mound suggest that the mound is Surface Type 2 material, in places mixed with Surface Type 1 basalt. THEMIS emissivity spectra for the mound units are consistent with a fairly dusty surface for all units (Figure 9).

[49] If instead the model included the Surface Type 1 (basaltic) end-member only, the origin of the mound layers would be consistent with interbedded lava flows or pyroclastic deposits of basaltic composition. Therefore the spectra of the mound layers were deconvolved again using the eight TES end-members and laboratory spectra of two sulfates (bloedite and glauberite). Unlike the low-albedo features in Gusev Crater, the availability of sulfates did not affect the inclusion of Surface Types 1 and 2 in deconvolution models for the mound layers. Therefore the mound appears to be a good spectral match to a combination of Surface Type 2 materials and surface dust.

[50] This is pertinent to the discussion of possible paleolake origin for the mound layers because the Surface Type 2 spectrum has been interpreted as either andesite or weathered basalt. Indeed, a single interpretation may not be appropriate for the whole of Mars. If interpreted as weathered basalt, these layers may represent a sedimentary rock composed of

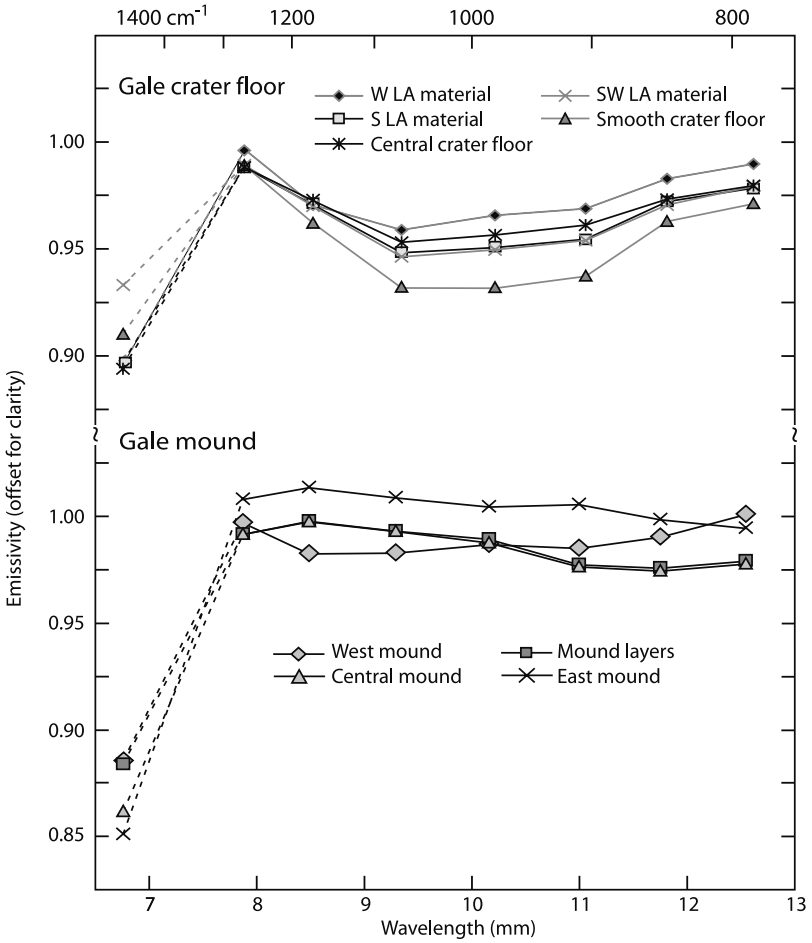

Figure 9. Mean THEMIS emissivity spectra for groups of ROIs defined for Gale Crater. Note that the emissivity displayed for bands 1 and 2 are apparent emissivity values, not true emissivity. Standard deviations for bands 3–9 are the height of the symbol or smaller. Standard deviations for bands 1 and 2 are twice the height of the symbol or smaller (with the exception of the W mound and W low-albedo ROI spectra, whose standard deviation is 2.3 times the height of the symbol).

weathered basalt or interbedded basaltic rocks that have undergone weathering. Either of these interpretations could support a lacustrine history for Gale Crater. However, the interpretation that the mound is composed of andesite cannot be discounted. Therefore, although this evidence does not disprove a possible paleolake origin, it does not exclusively support a paleolacustrine period for Gale Crater either.

5. Conclusions

[51] On the basis of our basin-scale examination of TES and THEMIS data within Aeolis quadrangle of Mars, we have learned the following:

[52] 1. Most of the surface of Gusev Crater is blanketed by a spectrally thick layer of dust that obscures the spectral signal from the surface. However, the low-albedo features appear to only have intermediate dust cover.

[53] a. When only provided the eight TES surface and atmospheric end-members, TES linear deconvolution models for the low-albedo features only included Surface Type 2 and surface dust end-members in significant amounts.

[54] b. When sulfates were provided in addition to the eight TES end-members, the TES linear deconvolution model for the least dusty crater floor ROI (crater floor 1) no longer included the Surface Type 2 end-member. Instead, the model included the Surface Type 1 basalt end-member with small (insignificant) amounts of sulfates.

[55] i. Although the sulfates are not present in significant amounts, their availability for the deconvolution modeling process may affect which Surface Type is included and provide a better match to what is observed at the surface of Mars.

[56] ii. When the sulfates are chosen in such low amounts and the differences in RMS errors are so small, it is difficult to say with certainty which model is better without available ground-truth results.

[57] c. THEMIS emissivity of the low-albedo features display very little spectral contrast, which prohibits identification of subtle spectral differences between Surface Types 1 and 2. Therefore these spectra are consistent with a mixture of either Surface Type 1 or 2 with dust.

[58] 2. On a broad scale, our view of Gale Crater via THEMIS is quite similar to our view from TES, with a fairly dust-free crater floor and a dustier mound.

[59] a. The crater floor represents a mixture of Surface Types 1, sometimes mixed with Surface Type 2.

[60] b. The dust mantling the central mound is variable in thickness, revealing some compositional information from

Table 4. Results From Deconvolution of TES Emissivity Data for LA Feature ROI in Gusev Crater, Using TES Spectral End-Members and Two Sulfates[a]

	S Low-Albedo Feature		N Low-Albedo Feature 1		N Low-Albedo Feature 2	
	8 TES Only	8 TES + 2 Sulf	8 TES Only	8 TES + 2 Sulf	8 TES Only	8 TES + 2 Sulf
Surface Type 1	6.0	**13.0**	0.0	0.0	0.0	0.0
Surface Type 2	9.0	0.0	**25.0**	**20.5**	0.0	0.0
Hematite	0.0	0.0	0.0	0.0	0.0	0.0
Surface dust	0.0	0.0	**22.0**	**30.5**	**35.5**	**43.0**
Bloedite	-	3.5	-	2.0	-	0.0
Glauberite	-	0.5	-	0.0	-	0.5
Dust Low-CO_2	**82.0**	**80.0**	**18.5**	**13.5**	**63.5**	**56.5**
Dust High-CO_2	0.0	0.0	**29.0**	**29.0**	0.0	0.0
H_2O Ice $Cloud_1$	0.0	0.0	0.0	0.0	0.0	0.0
H_2O Ice $Cloud_2$	2.5	3.5	6.5	5.5	1.5	0.0
Sum	99.5	100.5	101.0	101.0	100.5	100.0
Spectral RMS	0.00449	0.00386	0.00325	0.00309	0.00470	0.00470
ΔRMS	0.00063		0.00017		0.00001	
DCI value	0.943		0.941		0.943	
Interpretation	intermediate		intermediate		intermediate	
THEMIS interpretation	ST1 or ST2? + Dust		ST1 or ST2? + Dust		ST1 or ST2? + Dust	

[a]Values have been rounded to the nearest 0.5%. Numbers in bold indicate end-members used in significant amounts (>10–15%; see text). DCI value and interpretation are based on *Ruff and Christensen* [2002]. For THEMIS interpretation, ST1 is Surface Type 1; ST2 is Surface Type 2, Dust is surface dust.

some areas of the mound. According to TES data, the central mound appears to be a mix of Surface Types 1 and 2; the mound layers represent Surface Type 2 only.

[61] i. Because the models included Surface Type 2 spectral end-member, which has been variously interpreted as weathered basalt [*Wyatt and McSween*, 2002; *Kraft et al.*, 2003; *Ruff*, 2004] or andesite [*Bandfield et al.*, 2000a, 2000b; *Hamilton et al.*, 2001], we are not able to constrain how the mound layers were deposited (i.e., volcanic versus sedimentary deposition) within Gale Crater.

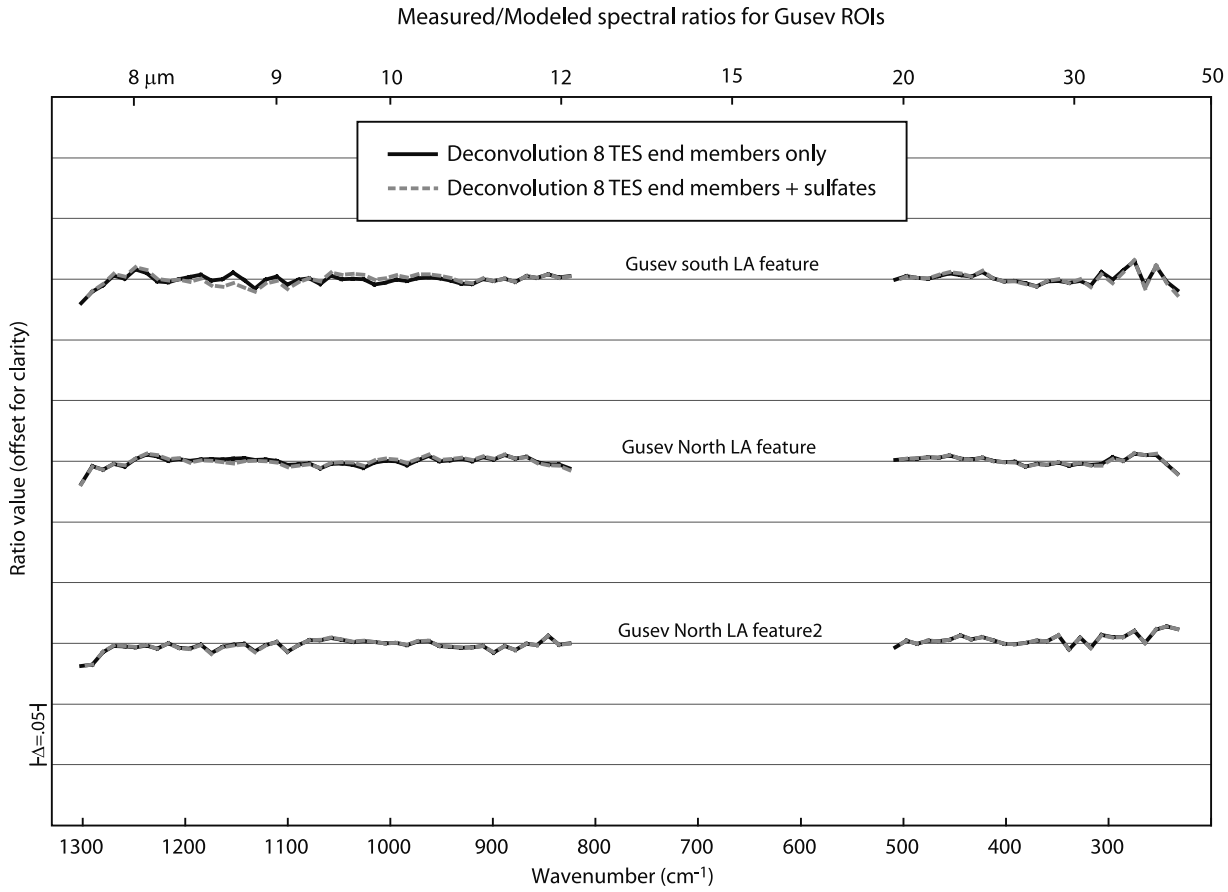

Figure 10. Measured-over-modeled spectral ratios from TES data of the ROIs of the low-albedo feature in Gusev Crater, offset 0.05 for clarity. The solid black lines are the measured-over-modeled ratios from deconvolution using the eight TES end-members only. The dashed gray lines are the measured-over-modeled ratios from deconvolution using the eight TES end-members plus two sulfate (bloedite and glauberite) spectra.

[62] ii. Surface Type 2 material present in mound layers might be consistent with numerous volcanic, sedimentary or volcanic-sedimentary petrogenesis and depositional scenarios.

[63] iii. THEMIS emissivity spectra are consistent with a dusty surface for the mound.

[64] 3. We have not found any unambiguous spectroscopic evidence of evaporites that might support a paleolacustrine origin for the surficial deposits in Gusev, Gale or other craters in the Aeolis quadrangle [*Stockstill*, 2005].

[65] a. Deconvolutions using the eight TES end-members model the measured spectra fairly well. Remnant absorptions revealed in spectral ratios of the measured over modeled spectra are related to additional atmospheric end-members (CO_2 vapor and/or water vapor), not mineral absorptions.

[66] b. Application of the carbonate indices [*Stockstill et al.*, 2005] to the TES spectra did not find any spectral signature of carbonates in these spectra.

[67] 4. Unlike previous global-scale searches for carbonates, this study focused on individual craters that may contain geomorphic evidence consistent with water entering and/or ponding within the crater. The nondetection of carbonates or other evaporites in these craters has several implications.

[68] a. Evaporite minerals may be present, but below the detection limits for these methods.

[69] b. Evaporites may be present but buried by dust or other rocks.

[70] c. Evaporite minerals may have been present in the past, but were not preserved due to erosional processes.

[71] d. It is also possible that a lake existed in one or several of the studied craters, but the lacustrine environment was not conducive to chemical sedimentation of carbonates.

[72] e. It is possible that the basin never contained ponded water or did not contain ponded water for a sufficient duration to produce extensive evaporite deposits.

[73] 5. At the spatial resolution of THEMIS data, the layers within the mound of Gale Crater are discernible near the limits of the data. We attempted to delineate any spectral patterns associated with these layers; however no appreciable spectral differences could be detected.

[74] a. It is possible that there is no spectral difference between the layers; the best way to determine whether or not real differences exist would be to examine warmer THEMIS data.

[75] b. Improvements to the THEMIS signal-to-noise ratio that would be achieved by acquiring additional data at earlier local times might permit us to discern more subtle spectral differences.

[76] 6. A number of spacecraft sent to Mars have produced evidence for sulfates in various locations on the Martian surface.

[77] a. The Viking Lander identified high sulfur contents in duricrusts at the Chryse site, which were interpreted as sulfate salt-enriched and cemented variations of the S-rich fines material [*Clark et al.*, 1982].

[78] b. The Mars pathfinder showed that the soils in Ares Vallis most likely representing a mix of a weathered basalt component and a "salt" component enriched in S, Cl, K and probably Na and Br [*McSween et al.*, 1999; *Newsom et al.*, 1999].

[79] c. The MER Spirit rover identified sulfates in soils and regolith of Gusev Crater [e.g., *Wang et al.*, 2005; *Arvidson et al.*, 2006].

[80] d. The MER Opportunity rover identified sulfates in the soils and outcrops of Meridiani Planum [*Clark et al.*, 2005].

[81] e. The Observatoire pour la Minéralogie, l'Eau, les Glaces, et l'Activité (OMEGA) mission identified outcrops containing hydrated sulfates in Valles Marineris, Margaritifer Sinus, and Terra Meridiani [*Gendrin et al.*, 2005] as well as calcium-rich sulfates near the north pole of Mars [*Langevin et al.*, 2005].

[82] Taken in this context, it is most likely that the nondetection of carbonates in this study is because the evaporite mineralogy of Mars is dominated by sulfates, rather than carbonates.

[83] **Acknowledgments.** This work benefited from discussions with or reviews by Vicky Hamilton, Melissa Lane, Josh Bandfield, Deanne Rogers, Will Koeppen, Jeff Byrnes, and Sara Martínez-Alonso. This study was supported by Arizona State University THEMIS subcontract 01-082 (H.Y.M.) and by the THEMIS Participating Scientist Program JPL contract 1241129 (J.E.M.). In addition, this material is based upon work supported by the National Aeronautics and Space Administration through the NASA Astrobiology Institute under Cooperative Agreement NNA04CC08A issued through the Office of Space Science.

References

Arvidson, R. E., et al. (2006), Overview of the Spirit Mars Exploration Rover Mission to Gusev Crater: Landing site to Backstay Rock in the Columbia Hills, *J. Geophys. Res.*, *111*, E02S01, doi:10.1029/2005JE002499.

Baker, V. R., and D. J. Milton (1974), Erosion by catastrophic floods on Mars and Earth, *Icarus*, *23*, 27–41.

Baldridge, A. M., J. D. Farmer, and J. E. Moersch (2004), Mars remote-sensing analog studies in the Badwater Basin, Death Valley, California, *J. Geophys. Res.*, *109*, E12006, doi:10.1029/2004JE002315.

Bandfield, J. L. (2002), Global mineral distributions on Mars, *J. Geophys. Res.*, *107*(E6), 5042, doi:10.1029/2001JE001510.

Bandfield, J. L., and M. D. Smith (2003), Multiple emission angle surface-atmosphere separations of Thermal Emission Spectrometer data, *Icarus*, *161*, 47–65.

Bandfield, J. L., P. R. Christensen, and M. D. Smith (2000a), Spectral data set factor analysis and end-member recovery: Application to analysis of Martian atmospheric particulates, *J. Geophys. Res.*, *105*, 9573–9587.

Bandfield, J. L., V. E. Hamilton, and P. R. Christensen (2000b), A global view of Martian surface compositions from MGS-TES, *Science*, *287*, 1626–1630.

Bandfield, J. L., T. D. Glotch, and P. R. Christensen (2003), Spectroscopic identification of carbonate mineral in the Martian dust, *Science*, *301*, 1084–1087.

Bandfield, J. L., D. Rogers, M. D. Smith, and P. R. Christensen (2004), Atmospheric correction and surface spectral unit mapping using Thermal Emission Imaging System data, *J. Geophys. Res.*, *109*, E10008, doi:10.1029/2004JE002289.

Bell, J. F., III, et al. (2004), Pancam multispectral imaging results from the Spirit Rover at Gusev Crater, *Science*, *305*, 800–806.

Brakenridge, G. R. (1990), The origin of fluvial valleys and early geologic history, Aeolis Quadrangle, Mars, *J. Geophys. Res.*, *95*, 17,289–17,308.

Cabrol, N. A. (1997), Early Amazonian lake in Gale Crater, Mars, *Lunar Planet. Sci.*, *XXVIII*, 191–192.

Cabrol, N. A., and E. A. Grin (1997), Hydrogeology and exobiology significance of Martian large crater lakes, paper presented at Conference on Early Mars: Geologic and Hydrologic Evolution, Physical and Chemical Environments, and the Implications for Life, Lunar and Planet. Inst., Houston, Tex.

Cabrol, N. A., and E. A. Grin (1999), Distribution, classification, and ages of Martian impact crater Lakes, *Icarus*, *142*, 160–172.

Cabrol, N. A., E. A. Grin, R. Landheim, R. O. Kuzmin, and R. Greeley (1998), Duration of the Ma'adim Vallis/Gusev Crater hydrogeologic system, *Icarus*, *133*, 98–108.

Cabrol, N. A., E. A. Grin, H. E. Newsom, R. Landheim, and C. P. McKay (1999), Hydrogeologic evolution of Gale crater and its relevance to the exobiological exploration of Mars, *Icarus*, *139*, 235–245.

Carr, M. H. (1987), Water on Mars, *Nature*, *326*, 30–35.

Carr, M. H. (1996), Formation of the Martian drainage system: Redistribution of groundwater in response to global topography and cold climates, in *Workshop on Evolution of Martian Volatiles*, *LPI Tech. Rep. 95-05*, pp. 7–9, Lunar and Planet. Inst., Houston, Tex.

Christensen, P. R. (1999), Calibration report for the Thermal Emission Spectrometer (TES) for the Mars Global Surveyor Mission, Mars Global Surveyor Project, Jet Propul. Lab., Pasadena, Calif.

Christensen, P. R., et al. (1992), Thermal Emission Spectrometer Experiment: Mars-Observer Mission, *J. Geophys. Res.*, *97*, 7719–7734.

Christensen, P. R., et al. (2000a), Detection of crystalline hematite mineralization on Mars by the Thermal Emission Spectrometer: Evidence for near-surface water, *J. Geophys. Res.*, *105*, 9623–9642.

Christensen, P. R., J. L. Bandfield, V. E. Hamilton, D. A. Howard, M. D. Lane, J. L. Piatek, S. W. Ruff, and W. L. Stefanov (2000b), A thermal emission spectral library of rock-forming minerals, *J. Geophys. Res.*, *105*, 9735–9739.

Christensen, P. R., et al. (2001), Mars Global Surveyor Thermal Emission Spectrometer experiment: Investigation description and surface science results, *J. Geophys. Res.*, *106*, 23,823–23,871.

Christensen, P. R., et al. (2003), Morphology and composition of the surface of Mars: Mars Odyssey THEMIS results, *Science*, *300*, 2056–2061.

Christensen, P. R., et al. (2004a), Initial results from the Min-TES experiment at the Spirit landing site in Gusev Crater, *Science*, *305*, 837–841.

Christensen, P. R., et al. (2004b), The Thermal Emission Imaging System (THEMIS) for the Mars 2001 Odyssey Mission, *Space Sci. Rev.*, *110*, 85–130.

Clark, B. C., A. K. Baird, R. J. Weldon, D. M. Tsusaki, L. Schnabel, and M. P. Candelaria (1982), Chemical composition of Martian Fines, *J. Geophys. Res.*, *87*, 10,059–10,067.

Clark, B. C., et al. (2005), Chemistry and mineralogy of outcrops at Meridiani Planum, *Earth Planet. Sci. Lett.*, *240*, 73–94.

Eugster, H. P. (1980), Geochemistry of evaporitic lacustrine deposits, *Annu. Rev. Earth Planet. Sci.*, *8*, 35–63.

Eugster, H. P., and L. A. Hardie (1978), Saline lakes, in *Lakes: Chemistry, Geology, Physics*, edited by A. Lernam, pp. 237–293, Springer, New York.

Farmer, J. D., and D. J. Des Marais (1999), Exploring for a record of ancient Martian life, *J. Geophys. Res.*, *104*, 26,977–26,995.

Feely, K. C., and P. R. Christensen (1999), Quantitative compositional analysis using thermal emission spectroscopy: Application to igneous and metamorphic rocks, *J. Geophys. Res.*, *104*, 24,195–24,210.

Forsythe, R. D., and J. R. Zimbelman (1995), A case for ancient evaporite basins on Mars, *J. Geophys. Res.*, *100*, 5553–5563.

Frey, H. V., S. E. H. Sakimoto, and J. H. Roark (1998), The MOLA topographic signature at the crustal dichotomy boundary zone on Mars, *Geophys. Res. Lett.*, *25*, 4409–4412.

Gellert, R., et al. (2004), Chemistry of rocks and soils in Gusev Crater from the Alpha Particle X-ray Spectrometer, *Science*, *305*, 829–832.

Gendrin, A., et al. (2005), Sulfates in Martian layered terrains: The OMEGA/Mars Express view, *Science*, *307*, 1587–1591.

Gillespie, A. R. (1985), Lithologic mapping of silicate rocks using TIMS, in *The TIMS Data Users' Workshop*, pp. 29–44, Jet Propul. Lab., Pasadena, Calif.

Gillespie, A. R. (1992), Spectral mixture analysis of multispectral thermal infrared images, *Remote Sens. Environ.*, *42*(2), 137–145.

Gillespie, A. R., A. B. Kahle, and R. E. Walker (1986), Color enhancement of highly correlated images. 1. Decorrelation and HSI contrast stretches, *Remote Sens. Environ.*, *20*, 209–235.

Golombek, M., et al. (2002), Downselecting of landing sites for the Mars Exploration Rovers, *Lunar Planet. Sci.*, *XXXIII*, Abstract 1245.

Greeley, R., and J. E. Guest (1987), Geologic map of the eastern equatorial region, Mars, *U.S. Geol. Surv. Misc. Invest. Ser.*, *Map I-1802–B*.

Green, A. A., M. Berman, P. Switzer, and M. D. Craig (1988), A transformation for ordering multispectral data in terms of image quality with implications for noise removal, *IEEE Trans. Geosci. Remote Sens.*, *26*, 65–74.

Grin, E. A., and N. A. Cabrol (1997), Limnologic analysis of Gusev crater paleolake (Mars), *Icarus*, *130*, 461–474.

Hamilton, V. E., and P. R. Christensen (2000), Determining the modal mineralogy of mafic and ultramafic igneous rocks using thermal emission spectroscopy, *J. Geophys. Res.*, *105*, 9717–9733.

Hamilton, V. E., M. B. Wyatt, H. Y. McSween Jr., and P. R. Christensen (2001), Analysis of terrestrial and Martian volcanic compositions using thermal emission spectroscopy, *J. Geophys. Res.*, *106*, 14,733–14,746.

Jones, B. F. (1965), The hydrology and mineralogy of Deep Springs Lake, Inyo County, California, *U.S. Geol. Surv. Prof. Pap.*, *502-A*, 56 pp.

Klingelhöfer, G., et al. (2005), MIMOS II on MER: One year of Mössbauer spectroscopy on the surface of Mars: From Jarosite at Meridiani Planum to Goethite at Gusev Crater, *Lunar Planet. Sci.*, *XXXVI*, Abstract 2349.

Kraft, M. D., J. R. Michalski, and T. G. Sharp (2003), Effects of pure silica coatings on thermal emission spectra of basaltic rocks: Considerations for Martian surface mineralogy, *Geophys. Res. Lett.*, *30*(24), 2288, doi:10.1029/2003GL018848.

Kuzmin, R. O., R. Greeley, R. Landheim, N. A. Cabrol, and J. D. Farmer (2000), Geologic map of the MTM-15182 and MTM-15187 quadrangles, Gusev Crater-Ma'adim Vallis region, *U.S. Geol. Surv. Geol. Invest. Ser.*, *I-2666*.

Landheim, R., N. A. Cabrol, R. Greeley, and J. D. Farmer (1994), Strategic assessment of Gusev crater as an exobiology landing site, *Lunar Planet. Sci.*, *XXV*, 845–846.

Lane, M. D. (2005), Evidence for aqueously precipitated sulfates in Northeast Meridiani using THEMIS and TES data, *Lunar Planet. Sci.*, *XXXVI*, Abstract 2180.

Lane, M. D., and P. R. Christensen (1997), Thermal infrared emission spectroscopy of anhydrous carbonates, *J. Geophys. Res.*, *102*, 25,581–25,592.

Lane, M. D., and P. R. Christensen (1998), Salt minerals predicted for Mars and their thermal infrared emission spectra, *Lunar Planet. Sci.* [CD-ROM], *XXIX*, Abstract 1102.

Langevin, Y., F. Poulet, J. P. Bibring, and B. Gondet (2005), Sulfates in the north polar region of Mars detected by OMEGA/Mars Express, *Science*, *307*, 1584–1586.

Lyon, R. J. P. (1965), Analysis of rocks by spectral infrared emission (8–25 μm), *Econ. Geol.*, *60*, 715–736.

Lyon, R. J. P., and K. Lee (1970), Remote sensing in exploration for mineral deposits, *Econ. Geol.*, *65*, 785–800.

Malin, M. C., and K. S. Edgett (2000), Sedimentary rocks of early Mars, *Science*, *290*, 1927–1937.

Martínez-Alonso, S., B. M. Jakosky, M. T. Mellon, and N. E. Putzig (2005), A volcanic interpretation of Gusev Crater surface materials from thermophysical, spectral, and morphological evidence, *J. Geophys. Res.*, *110*, E01003, doi:10.1029/2004JE002327.

Masursky, H. (1973), An overview of geological results from Mariner 9, *J. Geophys. Res.*, *78*, 4009–4049.

McCauley, J. F. (1974), White Rock: A Martian enigma, *NASA Spec. Publ.*, *329*, 170–171.

McSween, H. Y., Jr., et al. (1999), Chemical, multispectral, and textural constraints on the composition and origin of rocks at the Mars Pathfinder landing site, *J. Geophys. Res.*, *104*, 8679–8715.

McSween, H. Y., Jr., et al. (2004), Basaltic rocks analyzed by the Spirit Rover in Gusev Crater, *Science*, *305*, 842–845.

Milam, K. A., K. R. Stockstill, J. E. Moersch, H. Y. McSween Jr., L. L. Tornabene, A. Ghosh, M. B. Wyatt, and P. R. Christensen (2003), THEMIS characterization of the MER Gusev crater landing site, *J. Geophys. Res.*, *108*(E12), 8078, doi:10.1029/2002JE002023.

Milton, D. J. (1973), Water and processes of degradation on Martian landscape, *J. Geophys. Res.*, *78*, 4037–4047.

Morris, R. V., et al. (2004), Mineralogy at Gusev Crater from the Mössbauer Spectrometer on the Spirit Rover, *Science*, *305*, 833–836.

Morris, R. V., et al. (2005), Abundance and speciation of water and sulfate at Gusev Crater and Meridiani Planum, *Lunar Planet. Sci.*, *XXXVI*, Abstract 2239.

Mutch, T. A., R. E. Arvidson, J. W. Head III, K. L. Jones, and R. S. Saunders (1976), *The Geology of Mars*, 400 pp., Princeton Univ. Press, Princeton, N. J.

Newsom, H. E., J. J. Hagerty, and F. Goff (1999), Mixed hydrothermal fluids and the origin of the Martian soils, *J. Geophys. Res.*, *104*, 8717–8728.

Pelkey, S. M., and B. M. Jakosky (2002), Surficial geologic surveys of Gale Crater and Melas Chasma, Mars: Integration of remote-sensing data, *Icarus*, *160*, 228–257.

Pelkey, S. M., B. M. Jakosky, and P. R. Christensen (2004), Surficial properties in Gale Crater, Mars, from Mars Odyssey THEMIS data, *Icarus*, *167*, 244–270.

Ramsey, M. S., and P. R. Christensen (1998), Mineral abundance determination: Quantitative deconvolution of thermal emission spectra, *J. Geophys. Res.*, *103*(B1), 577–596.

Realmuto, V. J. (1990), Separating the effects of temperature and emissivity: Emissivity spectrum normalization, in *Proceedings of the Second TIMS Workshop*, pp. 23–27, Jet Propul. Lab., Pasadena, Calif.

Ruff, S. W. (2004), Spectral evidence for zeolites in the dust on Mars, *Icarus*, *168*, 131–143.

Ruff, S. W., and P. R. Christensen (2002), Bright and dark regions on Mars: Particle size and mineralogical characteristics based on Thermal Emission Spectrometer data, *J. Geophys. Res.*, *107*(E12), 5127, doi:10.1029/2001JE001580.

Ruff, S. W., et al. (2001), Mars' "White Rock" feature lacks evidence of an aqueous origin: Result from Mars Global Surveyor, *J. Geophys. Res.*, *106*, 23,921–23,927.

Sagan, C., O. B. Toon, and P. J. Gierasch (1973), Climatic change on Mars, *Science*, *181*, 1045–1049.

Salisbury, J. W., A. Wald, and D. D. Aria (1994), Thermal-infrared remote sensing and Kirchhoff's law: 1. Laboratory measurements, *J. Geophys. Res.*, *99*, 11,897–11,911.

Schneeberger, D. M. (1989), Episodic channel activity at Ma'adim Vallis, Mars, *Lunar Planet. Sci.*, *XX*, 964–965.

Schröder, C., et al. (2005), Weathering of basaltic rocks from the Gusev Plains up into the Columbia Hills from the perspective of the MER Mössbauer Spectrometer, *Lunar Planet. Sci.*, *XXXVI*, Abstract 2309.

Scott, D. H., and M. G. Chapman (1995), Geologic and topographic maps of the Elysium Paleolake basin, Mars, 1:500,000 scale, *U.S. Geol. Surv. Misc. Invest. Ser.*, *Map I-2397*.

Scott, D. H., E. C. Morris, and M. N. West (1978), Geologic map of the Aeolis Quadrangle of Mars (MC-23), *U.S. Geol. Surv. Misc. Invest. Ser.*, *Map I-1111*.

Sharp, R. P., and M. C. Malin (1975), Channels on Mars, *Geol. Soc. Am. Bull.*, *86*, 593–609.

Smith, M. D. (2002), The annual cycle of water vapor on Mars as observed by the Thermal Emission Spectrometer, *J. Geophys. Res.*, *107*(E11), 5115, doi:10.1029/2001JE001522.

Smith, M. D., J. L. Bandfield, and P. R. Christensen (2000), Separation of atmospheric and surface spectral features in Mars Global Surveyor Thermal Emission Spectrometer (TES) spectra, *J. Geophys. Res.*, *105*, 9589–9607.

Squyres, S. W., et al. (2004), The Spirit Rover's Athena Science Investigation at Gusev crater, Mars, *Science*, *305*, 794–799.

Stockstill, K. R. (2005), Analysis of Martian parental melts and thermal infrared studies of putative paleolake basins on Mars, Ph.D. dissertation, 260 pp., Univ. of Tennessee, Knoxville, Tenn.

Stockstill, K. R., J. E. Moersch, S. W. Ruff, A. Baldridge, and J. Farmer (2005), Thermal Emission Spectrometer hyperspectral analyses of proposed paleolake basins on Mars: No evidence for in-place carbonates, *J. Geophys. Res.*, *110*, E10004, doi:10.1029/2004JE002353.

Thomson, J. L., and J. W. Salisbury (1993), The mid-infrared reflectance of mineral mixtures (7–14 mm), *Remote Sens. Environ.*, *45*(1), 1–13.

Wang, A., et al. (2005), Sulfate deposition in regolith exposed in trenches on the plains between the Spirit landing site and Columbia Hills in Gusev Crater, Mars, *Lunar Planet. Sci.*, *XXXVI*, Abstract 2236.

Ward, A. W. (1979), Yardangs on Mars: Evidence of recent wind erosion, *J. Geophys. Res.*, *84*, 8147–8166.

Williams, S. H., and J. R. Zimbelman (1994), "White Rock": An eroded Martian lacustrine deposit (?), *Geology*, *22*, 107–110.

Wyatt, M. B., and H. Y. McSween Jr. (2002), Spectral evidence for weathered basalt as an alternative to andesite in the northern lowlands of Mars, *Nature*, *417*, 263–266.

Zimbelman, J. R., and H. H. Kieffer (1979), Thermal mapping of the northern equatorial and temperate latitudes of Mars, *J. Geophys. Res.*, *84*, 8239–8251.

P. R. Christensen, Department of Geological Sciences, Arizona State University, Tempe, AZ 85287, USA.

H. Y. McSween Jr., J. E. Moersch, and J. Piatek, Department of Earth and Planetary Sciences, University of Tennessee, Knoxville, TN 37996, USA.

K. R. Stockstill, HIGP/UH-NAI, University of Hawaii at Manoa, Honolulu, HI 96815, USA. (kstockst@higp.hawaii.edu)